Meissner-levitating magnets in superconductor-insulator composite traps

Pranger, Nathaniël

Meissner-levitating magnets in superconductor-insulator composite traps

THESIS

submitted in partial fulfillment of the
requirements for the degree of

MASTER OF SCIENCE
in
PHYSICS

Author :	Nathaniël Pranger
Student ID :	s2631016
Supervisor :	Prof. dr. ir. Tjerk Oosterkamp
2^{nd} corrector :	Dr. ir. Bas Hensen

Leiden, The Netherlands, July 16, 2025

Meissner-levitating magnets in superconductor-insulator composite traps

Nathaniël Pranger

Huygens-Kamerlingh Onnes Laboratory, Leiden University
P.O. Box 9500, 2300 RA Leiden, The Netherlands

July 16, 2025

Abstract

Levitating masses are a promising platform for highly sensitive gravity measurements and the eventual elucidation of quantum gravity. Small permanent magnets are commonly levitated in superconducting traps. However, an unpredictable coupling effect, tentatively named *flux trapping*, makes the magnets' oscillating modes inconsistent. We developed a new superconducting trap from superconducting tantalum powder mixed into an insulating epoxy resin. We record levitation after every cooldown, but oscillating modes depend strongly on the aluminium shielding around the trap, suggesting that flux penetrating the insulator poses fresh design challenges in shielding and thermalisation. We also manufactured a circular *racetrack* from the same material, around which magnets might be propelled. Although we did observe levitation, the magnet in the racetrack did not lift off with every cooldown. The magnet could not be moved a significant distance along the racetrack, indicating demand for more effective driving coils. When operational, this racetrack may serve as a periodic gravitational signal for future small-gravity measurements.

Contents

Chapter 1

Context

It is not currently understood how quantum systems interact with gravity. Can particles be gravitationally entangled? How does a massive particle in superposition distort spacetime? Fundamentally, can general relativity be expanded with or generalised into a quantum description? To explore these questions, the Quantum Limits project seeks to understand quantum systems of ever greater mass [1]. The dream experiment is the measurement of gravity generated by a massive superposition.

In the Oosterkamp Lab at LION, experiments are undertaken which advance gravity measurements to ever smaller masses. Previously, gravity has been measured between a milligram levitated magnet and a kilogram mass at half a metre removed [2]. Resonance between the magnet's oscillating modes and the rotating mass was exploited to achieve a force measurement of attonewtons. This research is being advanced in several ways. Two aspects are relevant for our project.
Firstly, it has been observed that the mode frequencies of the levitating magnet drift over time, challenging long-term gravitational coupling at resonance [3]. The hypothecated effect - *flux trapping* - which may cause this frequency change needs to be better understood.
Secondly, the next advance of the experiment would be to use a much smaller source mass. A much smaller source mass needs to be much closer to the test mass if the gravitational force is to be measured: it needs to move into the cryostat. We need to develop a system in which a levitated milligram mass traces a circular path.

Chapter 2

Theory

2.1 Meissner Effect

In this research, we levitated magnets in superconducting traps by means of the Meissner effect: the expulsion of magnetic fields from a superconductor. When a magnet is placed on a superconductor, the expulsion of its magnetic field causes a force on the magnet, counteracting gravity, allowing the magnet to hover in place. To understand this effect more deeply, we need a brief introduction to superconductors and the Meissner effect. Much of this is taken from Tinkham's *Introduction to Superconductivity* [4] chapter 2 and Dr. Kaveh Lahabi's lecture notes for the course *Superconductivity*.

2.1.1 Theory of type I superconductors

A common definition of a superconductor (SC) is "**a metal without electrical resistance**" [5]. Although this is broadly a true property of SCs, often a critically useful one, such a definition elides the quantum nature of SCs and fails to explain some of their most important phenomena. A better definition of an SC might be "**a macroscopic quantum entity in which charge distribution and magnetic field penetration are governed by a single wave function**". This definition will at least suffice to explain the system at hand in this research. The principle thing for us to understand is: when and how do SCs expel magnetic fields?

Perfect Diamagnetism

Materials which have a superconducting state transition into it below a given *critical temperature* T_C. For type I SCs (the only type discussed here), this temperature tends to be extremely low; for tantalum - the SC used in this research - it is 4 Kelvin [6]. Around T_C, the material's resistivity ρ shows a sharp decline and quickly becomes 0. That is extremely useful for high-current cables, for example, as Joule heating vanishes. But what effect does it have on external magnetic fields?

Normal, resistive, metals exhibit an opposition to changing magnetic fields by Lenz's Law: currents induced by a changing magnetic flux create a magnetic flux that opposes the change. This follows from Faraday's law of induction.

$$\varepsilon = -\frac{d\Phi}{dt} \tag{2.1}$$

The electromotive force can be understood as a voltage U induced on the charges in the circuit. It is the *current* which creates the opposing magnetic field, by the Ampère-Maxwell law

$$\boldsymbol{\nabla} \times \boldsymbol{B} = \mu_0 \boldsymbol{j} \tag{2.2}$$

$$\boldsymbol{j} = \frac{1}{\rho}\boldsymbol{E}$$

$$\rho \to 0$$

$$\boldsymbol{j} \to \text{arbitrarily big}$$

For a resistivity approaching zero, the current can become arbitrarily big, generating an arbitrarily strong response magnetic field, in principle cancelling the change in flux perfectly. This is called **Perfect Diamagnetism** and SCs do exhibit it. The problem is that this predicts no cancellation of *static* magnetic flux, or their expulsion during the SC phase transition, one of the most notable characteristics of SCs. To understand how static magnetic flux is expelled (and hence stable levitation made possible) requires a more fundamental treatment.

The Meissner Effect

The true Meissner effect - the repulsion of all magnetic flux by an SC - cannot be "derived" from a classical picture like we did for perfect diamagnetism, notes Tinkham [4]. The Meissner effect follows from Londons' second equation, a phenomenological equation describing magnetic fields and supercurrents in SCs, constructed from the quantum formulation of momentum in the ground state. Londons' second equation connects the curl of the supercurrent $\boldsymbol{j_s}$ to the magnetic field $\boldsymbol{B}$.

$$\boldsymbol{\nabla} \times \boldsymbol{j_s} = -\frac{n_s e^2}{m}\boldsymbol{B} \tag{2.3}$$

which combines with equation (2.2) to give

$$\nabla^2 \boldsymbol{B} = \frac{\boldsymbol{B}}{\lambda^2} \tag{2.4}$$

a differential equation of the magnetic field over space. What solution does this have for, say, a constant magnetic field $B_z(0)$ perpendicular to the SC's surface?

$$\frac{\partial^2 B_z(z)}{\partial z^2} = \frac{1}{\lambda^2} B_z(z)$$

$$\Rightarrow B_z(z) = B_z(0) e^{z/\lambda} \tag{2.5}$$

An exponential decay as we go deeper into the SC, with λ a characteristic decay length known as the **London Penetration Depth**. Notably, adding a constant magnetic field everywhere $B_z(z) \to B_z(z) + B_0$ does *not* remain a valid solution of the differential equation. Therefore, static magnetic fields are expelled; any magnetic field can only penetrate into the SC to depths on the order of λ. For tantalum this is around 0.15 µm [7], not a significant depth on the scale of our system.

The expulsion of magnetic fields means that the normal component of the magnetic field is always zero at the SC's surface (give or take λ). Therefore, a magnet close to an SC's surface will always have part of its field cancelled. How this translates into a repulsive force and levitation is explained in section 2.2.

2.1.2 Critical field

When the energy of an external magnetic field exceeds that of the SC phase transition, the SC returns to the normal state [4]. The value of this field is a material property but depends on temperature; for tantalum at 1.1 K it is (83.0 ± 0.4) mT. From this and the radius r and remanence B_r of the magnet, we can determine a minimum levitation height z such that the critical field is not exceeded.

$$B(z) = \left(\frac{z-r}{r}\right)^{-3} \frac{B_r}{2} < B_C \tag{2.6}$$

$$z > \left(\frac{B_r}{2B_C}\right)^{1/3} r + r$$

Which for B_r = 1.3 T and r = 0.5 mm yields $z > 1.5$ mm.

2.2 Magnetolevitation: The Infinite-Plane Approximation

When a magnet levitates in a superconducting trap, the Meissner effect shields magnetic flux from the SC. The magnetic field becomes zero at the SC interface, which can be understood as the sum of the fields of the real magnetic dipole and a (potentially infinite) number of image magnetic dipoles inside the SC [8]. The dipoles have a repulsive dipole-dipole interaction, which enacts a force on the magnet away from the SC.
To levitate the magnet, the SC must create a dipole-dipole interaction equal and opposite to gravity. We can simplify this model by making the SC fill half-space at $z < 0$. In this case, the real magnetic dipole and image dipoles must make $B_z = 0$ in the entire xy-plane, give or take the London penetration depth, which at these scales is negligible. The solution is that there is a single image dipole: the levitating magnet mirrored in the xy-plane. From this, a dipole-dipole Hamiltonian can be constructed which provides the equilibrium levitation height, the vertical translational mode, and the pitch rotational mode.

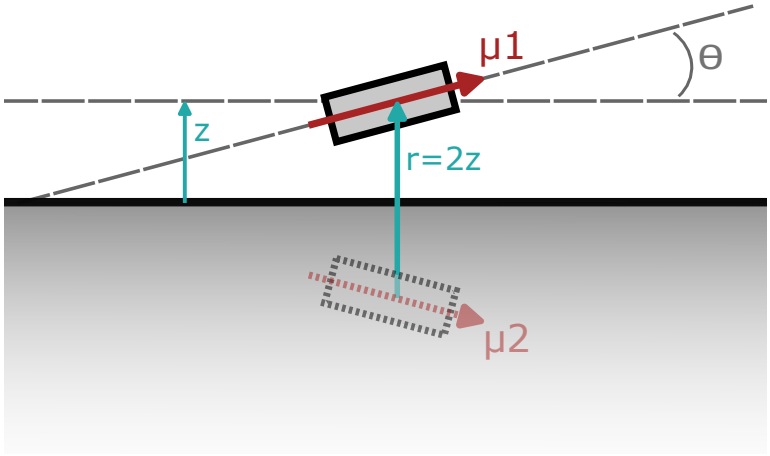

Figure 2.1: *Schematic of the infinite-plane model, with the levitated magnet μ_1 and the image dipole μ_2. Adapted from Dennis Uitenbroek [8].*

2.2.1 Hamiltonian

The image dipole $\boldsymbol{\mu_2}$ generates a magnetic field [9]

$$\boldsymbol{B_2}(\boldsymbol{r}) = \frac{\mu_0}{4\pi}\frac{1}{|\boldsymbol{r}|^3}(3(\boldsymbol{\mu_2}\cdot\hat{\boldsymbol{r}})\hat{\boldsymbol{r}} - \boldsymbol{\mu_2}) + \frac{2}{3}\mu_0\boldsymbol{\mu_2}\delta(\boldsymbol{r}) \tag{2.7}$$

which for the real dipole $\boldsymbol{\mu_1}$ at $\boldsymbol{r}$ gives the dipole-dipole Hamiltonian

$$H = -\boldsymbol{\mu_1}\cdot\boldsymbol{B_2}(\boldsymbol{r}) = -\frac{\mu_0}{4\pi}\frac{1}{|\boldsymbol{r}|^3}(3(\boldsymbol{\mu_1}\cdot\hat{\boldsymbol{r}})(\boldsymbol{\mu_2}\cdot\hat{\boldsymbol{r}}) - \boldsymbol{\mu_1}\cdot\boldsymbol{\mu_2}) - \mu_0\frac{2}{3}\boldsymbol{\mu_1}\cdot\boldsymbol{\mu_2}\delta(\boldsymbol{r}) \tag{2.8}$$

The final term ensures that $\boldsymbol{\nabla}\cdot\boldsymbol{B} = 0$ everywhere. It vanishes everywhere except at the location of the image dipole, so we can discard it. Furthermore, we know that

$$\begin{aligned}
\boldsymbol{\mu_1}\cdot\hat{\boldsymbol{r}} &= \mu\cos(\pi/2+\theta) = -\mu\sin\theta \\
\boldsymbol{\mu_2}\cdot\hat{\boldsymbol{r}} &= \mu\cos(\pi/2-\theta) = \mu\sin\theta \\
\boldsymbol{\mu_1}\cdot\boldsymbol{\mu_2} &= \mu^2\cos 2\theta = \mu^2(1-2\sin^2\theta) \\
|\boldsymbol{r}| &= 2z
\end{aligned}$$

so we write

$$H = \frac{\mu_0\mu^2}{32\pi z^3}(\sin^2\theta + 1) \tag{2.9}$$

for the two-dipole system. For the potential energy of the real dipole alone, this solution needs to be halved [8]. It will also be convenient to write μ in terms of the remanence B_r and volume of the magnet.

$$\mu = \frac{B_r V}{\mu_0} \tag{2.10}$$

Adding the gravitational potential $U_g = mgz$, we obtain the height- and angle-dependent potential energy of the levitating magnet

$$U_z = \frac{B_r^2 V^2}{64\pi\mu_0 z^3}(\sin^2\theta + 1) + mgz \tag{2.11}$$

2.2.2 Equilibrium height

To find the equilibrium height z_0, we start by fixing the equilibrium angle $\theta = 0$ and find the minimum of U_z with respect to z.

$$\frac{\delta}{\delta z}U_z = \frac{\delta}{\delta z}\left[\frac{B_r^2 V^2}{64\pi\mu_0 z^3} + mgz\right] = 0$$

$$-\frac{3B_r^2 V^2}{64\pi\mu_0 z^4} + mg = 0$$

$$z_0 = \left(\frac{3B_r^2 V^2}{64\pi\mu_0 mg}\right)^{1/4} \tag{2.12}$$

Note that, for a cylindrical or rectangular cuboid magnet of cross-section A and length l we have $V = Al$ and $m = \rho V$ where ρ is the material density. This gives us useful scaling laws.

$$z_0 \propto l^{1/4}$$

$$z_0 \propto A^{1/4} \propto d^{1/2}$$

With d the diameter. These scaling laws can quickly tell us what effect using a different magnet would have. For a $1 \times 1 \times 2$ mm NdFeB magnet ($B_r = 1.3\,T$; $\rho = 7500\,kgm^{-3}$) we find $z_0 = 4.8$ mm.

2.2.3 Vertical translational mode

We find the eigenfrequency of the z-mode through the 'spring constant' k_z. The spring constant is found by evaluating the second z-derivative of U_z at z_0.

$$k_z = \frac{\delta^2}{\delta z^2} U_z \bigg|_{z_0} = \frac{\delta^2}{\delta z^2} \left(\frac{B_r^2 V^2}{64\pi\mu_0 z^3} + mgz \right) \bigg|_{z_0} = \frac{3B_r^2 V^2}{16\pi\mu_0 z_0^5} \tag{2.13}$$

Then we use the eigenfrequency of a mass-spring system

$$f = \frac{\omega}{2\pi} = \frac{1}{2\pi}\sqrt{\frac{k}{m}}$$

to find the eigenfrequency of the vertical oscillation.

$$f_z = \frac{1}{2\pi}\sqrt{\frac{3B_r^2 V^2}{16\pi\mu_0 m z_0^5}} \tag{2.14}$$

Again, we find useful scaling laws for a cylindrical or rectangular cuboid magnet:

$$f_z \propto z_0^{-5/2}$$
$$f_z \propto l^{3/8}$$
$$f_z \propto A^{3/8} \propto d^{3/4}$$

For our magnet we find $f_z = 14.6$ Hz.

2.2.4 Horizontal translational modes

The horizontal translational modes can be estimated by modelling the magnet as being located between two infinite vertical superconducting surfaces [10]. There are then not just one or two image dipoles, but an infinite number, since image dipoles in one SC will themselves be reflected in the other SC, as is shown in this schematic from Francis Headley.

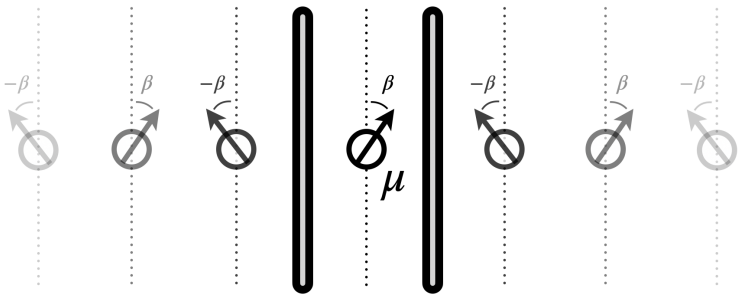

Figure 2.2: *A schematic of the infinite image dipoles when a magnet is between two infinite SC surfaces. Taken directly from Francis Headley [10].*

The x-dependent potential U_x of the magnet can be derived in essentially the same way as the z-dependent shown earlier, although accounting for the infinite image dipoles results in a more complicated expression. For a magnet a distance b from both surfaces, the potential energy is

$$U_x(x) = \frac{\mu_0 \mu^2}{8\pi} \left(\frac{\zeta(3)}{32b^3} + \sum_{n \epsilon \mathbb{Z}} \frac{1}{|2x - 4nb - 2b|^3} \right) \tag{2.15}$$

Where $\zeta(3)$ is the Riemann zeta function of 3. From this the resonance frequency can be found

$$f_x = \frac{1}{2\pi} \sqrt{\frac{1}{m} \frac{\partial^2 U_x}{\partial x^2}} \bigg|_{x=0} = \sqrt{\frac{93}{1024} \frac{\zeta(5)}{\pi^3} \frac{\mu_0 \mu^2}{b^5 m}} \tag{2.16}$$

The semiminor axis of our trap is about 5.5 mm long, so b = 5.5 mm. This gives f_x = 14.6 Hz. Note that this coincidentally is the same value as for f_z. We expect the experiment to behave differently enough from theory that degeneracy is not an issue. Corrections introduced in section 2.2.7 also differentiate these two frequencies. Note finally that this is a kind of lower bound of the frequency. The trap has a rounded shape, meaning that b is smaller the deeper in the trap the magnet levitates.

Headley's equations can also be used to find the y-mode, that being the other horizontal translational mode. The only adjustments are to set the angle to $\beta_0 = 90^\circ$ *. This yields

$$f_y = \sqrt{\frac{93}{512} \frac{\zeta(5)}{\pi^3} \frac{\mu_0 \mu^2}{b^5 m}} \tag{2.17}$$

Plugging in the semimajor axis b = 6.95 mm gives f_y = 11.5 Hz.

2.2.5 Rotational modes

The models as shown in figures 2.1 and 2.2 can be used to find the pitch-rotational mode (denoted by θ) and the yaw-rotational mode (denoted by β). The roll-rotational mode has nothing to do with the Meissner effect, but rather comes from the asymmetric mass distribution of the magnet, which we ensured by applying a line of resin along one side. This mode is

*Angle-dependence is not shown in equation 2.15, but this angle adjustment ultimately results in $\frac{\partial^2 U_x}{\partial x^2}$ being doubled. Cf Headley [10] if necessary.

not estimated theoretically here.

The θ and β rotational eigenfrequencies are found from the second derivatives of the potential energy to these angles [8] [10].

$$f_i = \frac{1}{2\pi}\sqrt{\frac{k_i}{I_i}} \tag{2.18}$$

$$k_\theta = \left.\frac{\partial^2 U_z}{\partial\theta^2}\right|_{z=z_0,\theta=0} = \frac{B_r^2 V^2}{32\pi\mu_0 z_0^3} \tag{2.19}$$

$$k_\beta = \left.\frac{\partial^2 U_x}{\partial\beta^2}\right|_{x=0,\beta=0} = \frac{\zeta(3)}{32\pi}\frac{B_r^2 V^2}{\mu_0 b^3} \tag{2.20}$$

The respective moments of inertia happen to be the same. For a 1x1x2 mm NdFeB rectangular prism, we have

$$I_\theta = I_\beta = \frac{15\,\mathrm{mg}}{12}((1\,\mathrm{mm})^2 + (2\,\mathrm{mm})^2) = 6.25\times10^{-12}\,\mathrm{kgm}^2 \tag{2.21}$$

Taking the equilibrium height and trap dimensions as before, this yields $f_\theta = 44.3\,\mathrm{Hz}$ and $f_\beta = 39.6\,\mathrm{Hz}$.

2.2.6 Tangential mode in a tilted racetrack

In the racetrack, the magnet is in principle free to move along its circular path when the racetrack is perfectly level. We can put the racetrack (indeed the entire cryostat) at an angle, in which case the magnet should oscillate pendulum-like around the lowest point. The frequency of this tangential mode can be estimated, since for small displacements from the lowest point, the tangential component of gravity is a linear restoring force. In this regime, the slope α is small, so we approximate

$$F_{g,\parallel} = -\sin(\alpha)mg \approx -\alpha mg = -\arctan(\frac{dz}{dx})mg \approx -\frac{dz}{dx}mg \tag{2.22}$$

The value of $\frac{dz}{dx}$ can be found from the geometry of the path.

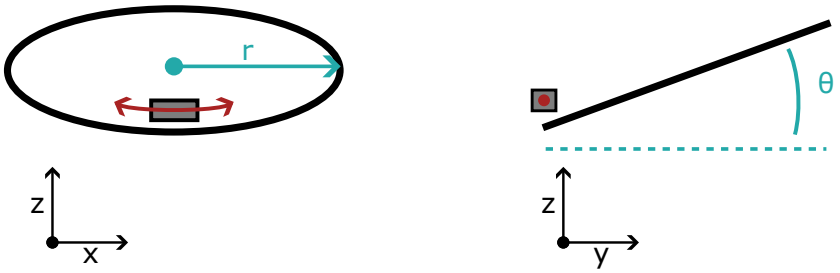

Figure 2.3: *Schematic of the circular path along the racetrack, seen from the front and the side.*

The circular path with radius r and angle θ to the horizontal is the intersection of a sphere with that radius and a plane at that angle. We centre the path at the origin without loss of generality. It has the equation

$$x^2 + z^2\left(1 + \frac{1}{\tan^2\theta}\right) = r^2$$

and therefore around the lowest point

$$z = -\sqrt{\frac{r^2 - x^2}{1 + 1/\tan^2\theta}}$$

Taking the derivate $\frac{dz}{dx}$ yields

$$\frac{dz}{dx} = \frac{x}{1 + 1/\tan^2\theta}\sqrt{\frac{(1 + 1/\tan^2\theta)/r^2}{1 - x^2/r^2}}$$

Since $x^2/r^2 << 1$ and $1 << 1/\tan^2\theta$ we approximate

$$\frac{dz}{dx} = \frac{x\tan\theta}{r}$$

Finally, substitution into equation (2.22) yields

$$F_{g,\parallel} = -\frac{mg\tan\theta}{r}x \tag{2.23}$$

This has the form of Hooke's law with spring constant

$$k = \frac{mg\tan\theta}{r} \tag{2.24}$$

From which we can find the tangential mode frequency

$$f_{\tan} = \frac{1}{2\pi}\sqrt{\frac{k}{m}} = \frac{1}{2\pi}\sqrt{\frac{g\tan\theta}{r}} \tag{2.25}$$

For example, if the cryostat is at 1 degree to the horizontal (a typical value) and we plug in the racetrack radius r = 27 mm, we find

$$f_{\tan} = \frac{1}{2\pi}\sqrt{\frac{9.81\,\mathrm{ms}^{-2}\cdot\tan(1^\circ)}{27\,\mathrm{mm}}} = 0.4\,\mathrm{Hz}$$

2.2.7 Adjustments for composite trap

Speculative proposal

Since SC-powder composite traps are new, we want to make appropriate adjustments to the model of the magnet's levitation height and mode frequencies. The boundary condition in the infinite-plane approximation - zero normal B-field at the superconducting surface - is no longer valid since the magnetic field may penetrate the bulk insulator. Therefore, it is impossible to arrive at a new model starting from this boundary condition. Rather, we iterate on the previous result.

We tentatively propose two corrections to the magnetic dipole moment μ of the image dipole. Firstly, since μ is proportional to the volume of the magnet, we suggest scaling μ with the volume fraction φ_{sc} of superconducting material in the composite. Secondly, the Meissner effect allows for magnetic fields to 'flow' around superconducting particles, in contrast to an infinite plane. Consider the analogue to air drag. We propose an equivalent 'drag coefficient' c_χ for the magnetic susceptibility χ to which μ is proportional.

Together, our corrections change μ or equivalently the volume of the image dipole for a given magnet volume, which returns in the equations as the substitution

$$V^2 \to V\varphi_{sc}c_\chi V = \varphi_{sc}c_\chi V^2 \tag{2.26}$$

which has the following consequences for the equilibrium height and translational eigenfrequencies:

$$z_0 \to (\varphi_{sc}c_\chi)^{1/4} z_0$$
$$f_z \to (\varphi_{sc}c_\chi)^{-1/8} f_z$$

$$f_i \to (\varphi_{sc} c_\chi)^{1/2} f_i \,;\, i \in \{x, y\}$$

Our composite trap had 18 percent superconducting powder by volume, and for spherical particles we use a coefficient $c_\chi = 0.3$, together giving the adjusted $z_0 = 2.3\,\text{mm}$, $f_z = 21.0\,\text{Hz}$, $f_x = 3.4\,\text{Hz}$ and $f_y = 2.7\,\text{Hz}$.

2.3 Dissipation Mechanisms

Below is an overview of the different mechanisms by which the oscillation of the magnet may be damped. All estimations of Q factors pertain to the z-translational mode of the magnet made of two 1x1x1 mm NdFeB cubes. Resonance frequencies are taken from those observed in the actual experiment. Oscillation amplitudes are estimated based on measured voltages in combination with a simplified geometry of the magnet and pickup coil.

Damping due to air drag

The cryostat has an ultra-high vacuum with a typical pressure of 10^{-8}mbar. We put holes in the lids of the experiments so the inside was under the same vacuum. At these pressures, drag is negligible.

Eddy current damping at the SC's surface

It is a matter of discussion whether the magnetic field that penetrates an SC's surface up to the London penetration depth induces dissipative currents. For this reason, no estimation is made here of the energy loss that such dissipative currents would cause. However, as this experiment uses powdered superconducting tantalum, which has a much larger surface area than a bulk SC, it is a relevant open question for future iterations of this method.

Eddy current damping within the magnet

As the magnet oscillates, it moves through the magnetic field of the image dipole. Since the magnet is itself a conductor, this generates dissipative eddy currents within the magnet. For simplicity, the calculations have been made for a cylindrical magnet.

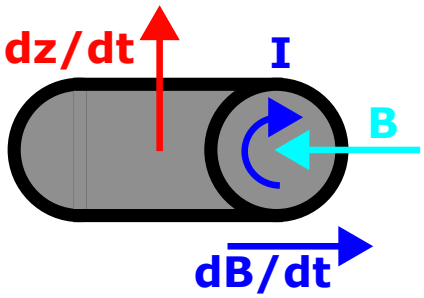

Figure 2.4: *Schematic of the changing magnetic field and the induced current as the magnet moves upward during its oscillation.*

As the magnet oscillates, the flux Φ from the magnetic field B through the magnet's circular area A changes. The induced voltage is

$$U_{\text{ind}} = -\frac{d\Phi}{dt} = -A\frac{dB}{dz}\frac{dz}{dt} = \frac{A}{\mu}\frac{dU_B}{dz}v_z = \frac{A}{\mu}F_B v_z \tag{2.27}$$

Since the magnet is levitating, the force due to the magnetic field gradient F_B is equal to the force of gravity $F_g = mg$ [†], so we can write

$$U_{\text{ind}} = \frac{mgv_z A}{\mu} \tag{2.28}$$

The Joule damping is then

$$P = \frac{U^2}{R} = \frac{(mgA/\mu)^2}{R}v_z^2 \tag{2.29}$$

To find the energy loss per oscillation cycle, we use the average vertical velocity over a cycle $\langle v_z^2 \rangle = (2\pi f_z)^2 Z^2/2$ for oscillation amplitude Z. We find

$$\Delta E_{\text{cycle}} = \frac{\langle P \rangle}{f_z} = 2\pi^2 f_z Z^2 \frac{(mgA)^2}{\mu^2 R} \tag{2.30}$$

The energy of the oscillation is

$$E = \frac{1}{2}k_z Z^2 = 2\pi^2 m f_z^2 Z^2 \tag{2.31}$$

so we conclude that the upper bound of the Q factor due to eddy current damping in the magnet is given by the expression

[†]Of course, the net force is only zero on average. We've also done the proper calculation where we integrate the net force over an oscillation, but the correction is tiny for any reasonable oscillation amplitude.

$$Q = 2\pi \frac{E}{\Delta E} = \frac{2\pi f_z \mu^2 R}{m g^2 A^2} \tag{2.32}$$

For a cylindrical NdFeB magnet with radius 0.5 mm and length 2 mm, we have the following values.

$$\mu = \frac{B_r V}{\mu_0} = 0.001\,63\,\mathrm{Am}^2$$

$$R = \rho \frac{l}{A} = 1.4 \times 10^{-6}\,\Omega\,\mathrm{m} \frac{\pi \cdot 0.5\,\mathrm{mm}}{0.5\,\mathrm{mm} \cdot 2\,\mathrm{mm}} = 0.0022\,\Omega$$

$$m = 11.8\,\mathrm{mg}$$

$$A = \pi r^2 = 7.85 \times 10^{-7}\,\mathrm{m}^2$$

Taking $f_z = 21\,\mathrm{Hz}$ from section 2.2.7, we finally obtain $Q = 1.1 \cdot 10^9$.

Joule damping in the pickup coil circuit

This experiment uses copper pickup coils, which are not superconducting at any practical temperature. Consequently, the induced currents in the pickup coils are dissipative. These can limit the Q factors significantly. The energy loss is due to Joule heating:

$$P = U_{\mathrm{total}} I_{\mathrm{total}} = \frac{U_{\mathrm{total}}^2}{R_{\mathrm{total}}} \tag{2.33}$$

The total voltage is the voltage amplitude as measured by the lock-in amplifier, divided by the pre-amplifier gain where necessary. The value of the total resistance depends on the measurement configuration. If the pickup coil is used only for measurement, the resistance is dominated by the impedance of the pre-amplifier. If the pickup coil is simultaneously serving as the driving coil, the resistance is that of the driving circuit, normally dominated by a resistor of 1 kΩ.
The energy loss over a period of oscillation is then

$$\Delta E = \int_0^{1/f} P dt = \frac{U_{\mathrm{total}}^2}{2 f R_{\mathrm{total}}} \tag{2.34}$$

The energy of the oscillation is

$$E = 2\pi^2 m f_z^2 Z^2$$

With Z the amplitude of the z-translational mode and f_z its frequency. The amplitude cannot be measured directly, but must be estimated from

the measured voltage and a simplified geometry. These geometries are different for the trap and the racetrack. Each gives a different relationship between oscillation amplitude and measured voltage, the derivations of which can be found in Appendix A.

- Trap

$$U_{\text{signal}} \approx \sin 2\theta \frac{3\pi B_r r^3}{2d^4} ANf_z Z \approx 4.5 \cdot 10^{-4}\, Vm^{-1}Hz^{-1} \cdot f_z \cdot Z \quad (2.35)$$

- Racetrack

$$U_{\text{signal}} \approx \cos\theta \frac{3\pi B_r r^3}{d^4} ANf_z Z \approx 7.5 \cdot 10^{-4} Vm^{-1}Hz^{-1} \cdot f_z \cdot Z \quad (2.36)$$

These coupling constants in $Vm^{-1}Hz^{-1}$ can be called $\kappa \overset{\text{def}}{=} \frac{U_{\text{signal}}}{f_z Z}$. Hence, the expression for the Q factor reduces to

$$Q = 2\pi \frac{E}{\Delta E} = \frac{4\pi^3 m(U/\kappa)^2}{U^2/2fR} = \frac{8\pi^3 mRf}{\kappa^2} \quad (2.37)$$

Which for a typical z-mode frequency of 20 Hz and a driving circuit resistance of 1 $k\Omega$ gives $Q = 3.6 * 10^8$ for the trap and $Q = 1.3 * 10^8$ for the racetrack. This method is also applicable to other modes, although coupling constants require fresh geometrical approximations.

Eddy current damping in surrounding metals

In SC-insulator composite traps, there is a non-zero magnetic field from the levitating magnet which can reach metals outside of the trap. Firstly, because the lid of the trap is made of an insulator (in this case 3D-printed PLA). In this aspect the new traps are no different than, say, the Zeppelin experiment [2]. Secondly, the resin-tantalum composite permits some flux to penetrate to the outside. In effect, it has a magnetic susceptibility $-1 < \chi < 0$.

A simulation by Dr. Bas Hensen shows that a superconducting trap with $\chi = -0.1$ allows a significant amount of flux to penetrate.

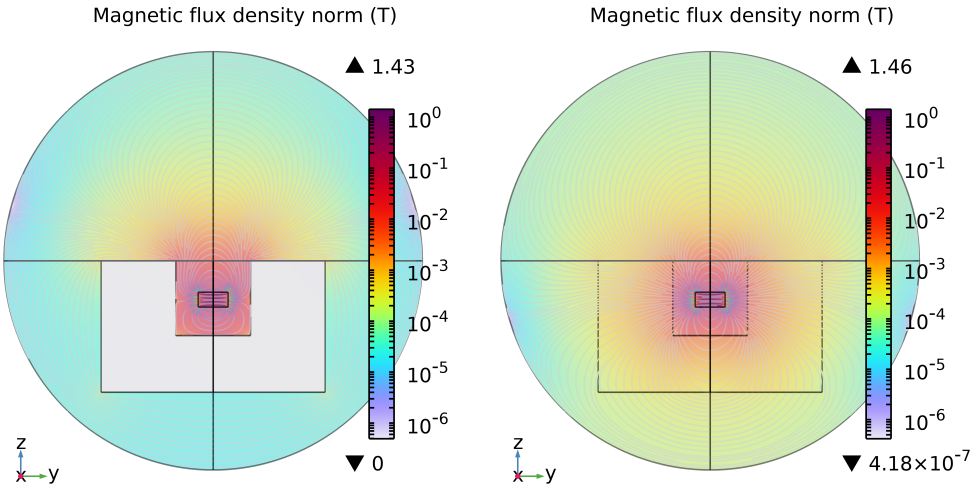

Figure 2.5: *(L) Simulation of a trap made from bulk Type I SC. (R) Simulation of a trap with χ = -0.1. Although the magnetic field decays exponentially in the latter, a significant amount of flux penetrates.*

To avoid the induction of dissipative currents, the experiments were shielded by aluminium (see sections 3.1.3 and 3.2.3). In the case of the trap, the copper mixing chamber plate of the cryostat was about 2 cm below the magnet, with only the resin-tantalum composite and a vacuum in between. In the case of the racetrack, there was aluminium shielding all around the racetrack. In principle, this all but eliminates dissipative currents in both experiments. The abundant presence of bulk type-I SC does of course reintroduce the risk of flux trapping, which is discussed in section 2.4.3.

2.4 Flux Trapping

2.4.1 Speculated model of the phenomenon

Flux trapping is a hypothecated effect in type I SCs. Its description has been necessitated by inconsistencies and changes over time of magneto-levitating systems. In the hypothesis, lines of magnetic flux become trapped in between superconducting grains of the bulk SC as it transitions to its SC state. The model below illustrates the effect as the SC cools below T_C and the magnet lifts off.

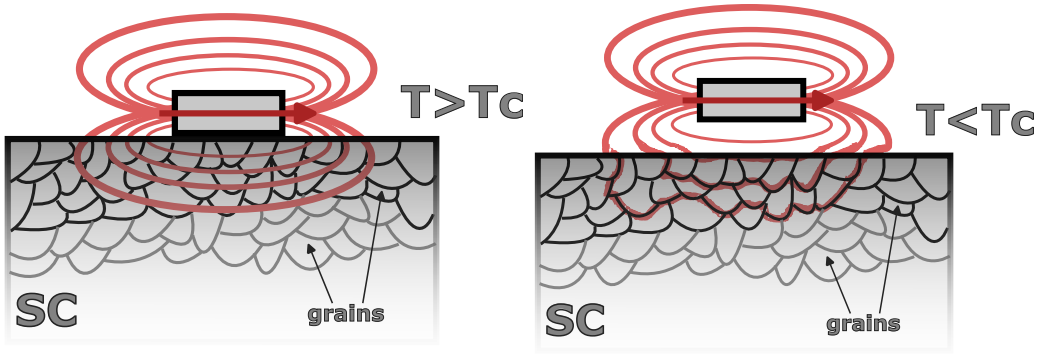

Figure 2.6: *Model of flux trapping in a bulk SC. As the SC cools below T_C, the magnet lifts off but magnetic flux lines becomes trapped between SC grains. Adapted from Lars Seldenthuis [11].*

It should be acknowledged that SCs are not traditionally understood to consist of grains, nor is it known whether these SC grains would be the same as the grains of the metal lattice. The consequence of flux trapping is not entirely understood. Measurements of the Zeppelin project have shown two telling effects:

1. Each time the system is cooled below the T_C of the SC, the mode frequencies of the magnet are significantly and unpredictably different.
2. Over time, as the system is kept below the T_C, the mode frequencies slowly decrease [3].

These observations suggest that (1) flux trapping strongly depends on conditions during the SC phase transition, such as the locations of grains, impurities, or the magnet. They also indicate that (2) flux trapping has a 'half life'. As flux escapes the SC, the coupling spring constant between the SC and the magnet decreases, causing a lowering of mode frequencies. It is not yet clear whether flux trapping is dissipative, or only modifies the coupling. Comparisons of Q factors may elucidate this.

2.4.2 Why might composites have less flux trapping?

The conception of this research was a thought from Tjerk Oosterkamp: "What if flux trapping can be reduced by using an SC trap made from powder?". Between the SC powder particles, there is an insulator. Through the insulator, magnetic field lines can move freely. Might some lines still

become trapped in the powder particles? There are two reasons to believe flux trapping would be greatly reduced.

1. If the powder particles are on average smaller than SC grains, flux trapping is *impossible* in most particles.
2. If flux trapping has a half-life, the half-life would be much shorter in the powder trap, since the average 'escape path' is much shorter.

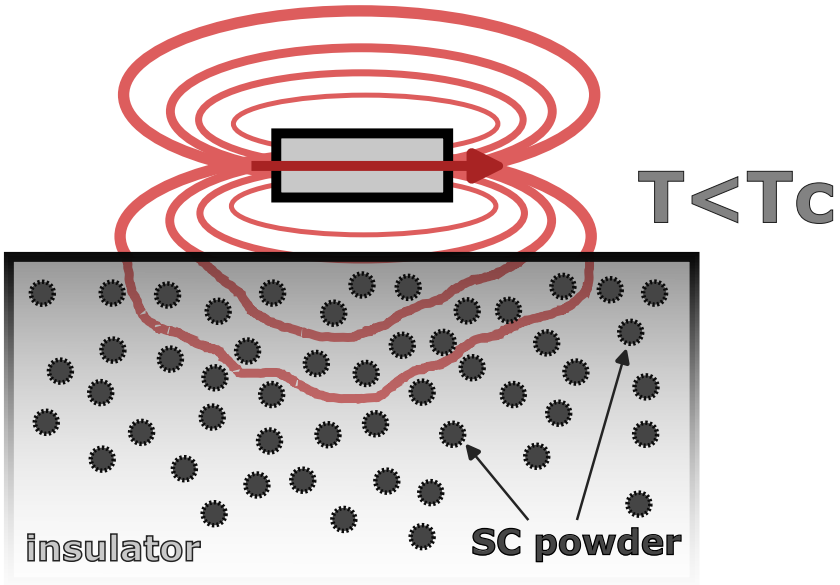

Figure 2.7: *A model of levitation above a composite trap. Field lines move around the powder particles, and can do so freely in 3D.*

2.4.3 Risks and considerations

We have explored the idea of composite traps in the hope of reducing flux trapping, but potential drawbacks need to be considered also.

Would the magnet even levitate?

Since such composite traps are - as far as we know - new, it is not known whether they could even support a levitating magnet. By our estimation, there is a mechanism which would allow levitation. It is true that the trap is not one bulk SC, and therefore the boundary condition of zero normal field at the trap's surface does not hold. The foundation of the image dipole model appears lost. However, each powder particle will expel the

tiny amount of flux at its surface. This effectively means that reflected behind each powder particle is a tiny image dipole. The interaction between the magnet with each of these millions[‡] of image dipoles is repulsive, constituting a net force away from the trap surface. Given a sufficient volume percentage of SC powder and a sufficiently thick layer of composite, levitation might be possible.

Would flux penetrating out of the trap cause problems?

As discussed in section 2.3, simulations suggest that a significant amount of flux can penetrate outside of a composite trap. If there are any non-SC metals directly outside of the trap, there will be eddy current damping. At the same time, the thermalisation from the cryostat plate to the trap goes through the shielding. The trap should be thermalised to its SC temperature before the shielding becomes SC; in its SC state the shielding conducts heat very poorly. The metals used for shielding and thermalisation should therefore be an SC with a lower T_C than tantalum, but achievable by the cryostat. Aluminium works, with $T_C = 1.2$ K. However, the whole point of the composite trap is to eliminate flux trapping. Surrounding such a trap with bulk type-I SC would be foolish: flux would get trapped in it. The SC metal used for shielding should therefore be kept as far away from the trap as possible, while direct thermalisation should be done with an electric insulator. This was implemented for the racetrack towards the end of this research, as explained in section 3.2.3.

[‡]A tantalum particle with a 74 µm diameter (a.k.a. 200 mesh) has a mass of about 3.5 µg. In 18 g of powder, therefore, there are about 5 million particles.

Chapter 3

Methods

3.1 Powder Trap Fabrication

3.1.1 Design and materials

The geometry of the powder trap is adapted from that used in the Zeppelin experiment [2]. The trap is elliptical, rather than circular, in the xy-plane to avoid degeneracy of the x and y translational modes. The bottom of the trap is rounded so the magnet-to-SC distance changes smoothly depending on levitation height, and to make sure the magnet returns to a central position when landing.
We 3D-printed a mould, into which silicon was cast. The cast silicon was in turn the mould for the final trap design.

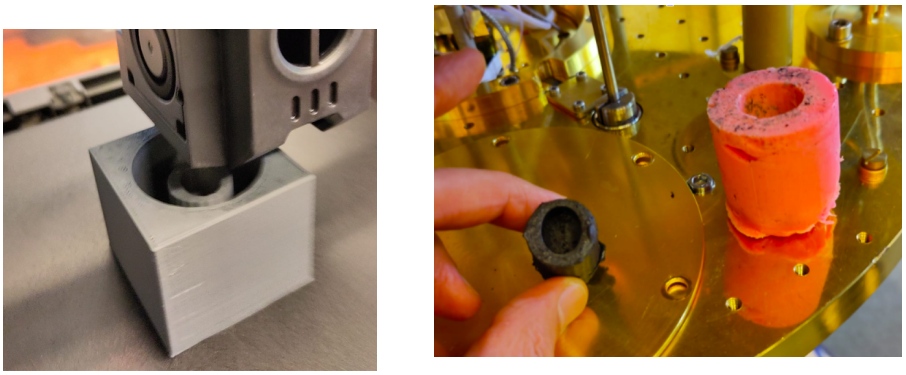

Figure 3.1: *(L) The 3D-printed mould of the trap. (R) The trap held beside its silicon trap. Photo credit: Tjerk Oosterkamp*

The materials of the trap are Loctite® Stycast 2850FT with CAT 24LV catalyst in 100:8 mass ratio - hereafter referred to as Stycast - and 200 mesh tantalum powder. After the Stycast was mixed, as much tantalum powder as possible was added while maintaining a mixable and pourable viscosity. This turned out to be 62 mass-percent or 18 volume-percent tantalum in the final mixture. The mixture was cast into the silicon mould and placed into a vacuum oven, where at 60 °C a vacuum was repeatedly pulled and then air leaked back in, causing the mixture to release gas. This degassing process was repeated for about 30 minutes, until few bubbles remained. Then the mixture was left to harden at 60 °C for 2 hours. After another hour for cooling, the Stycast-tantalum trap was easily released from its mould.

3.1.2 The magnet

The levitated magnet consists of two 1x1x1 mm NdFeB cubes, with a total mass of approximately 15 mg. To prevent free rolling around the long axis, we put a line of Stycast along the length of the magnet on one side.

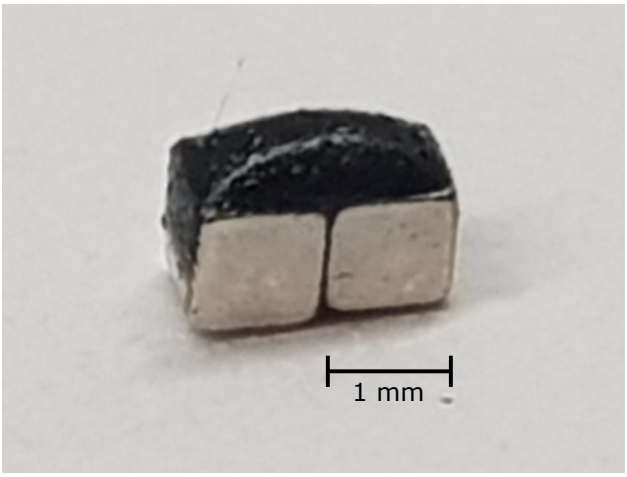

Figure 3.2: *The magnet of two 1x1x1 mm NdFeB cubes. This is in fact the magnet levitated in the racetrack, but the trap magnet was constructed by exactly the same method.*

3.1.3 Fastening, thermalisation, and shielding

The trap was fastened with Stycast to a copper bracket. For better thermalisation, copper foil was wrapped around the trap and bracket, again adhering with a thin layer of Stycast. Both the copper bracket and foil

were replaced with aluminium for later experiments to reduce eddy current damping (see section 2.3).

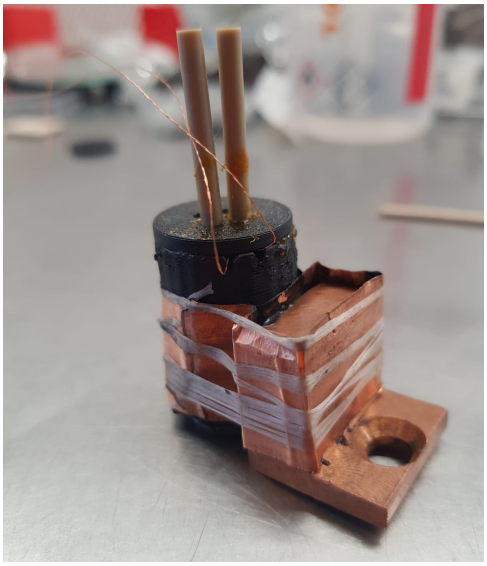

Figure 3.3: *The powder trap with its original copper cladding.*

The trap was shielded with a cylinder of $\mu-$metal and a lid of thick aluminium foil. There was no shielding directly below the trap, but the bracket ensured a centimetre of vacuum between the trap and the mixing chamber plate.

Figure 3.4: *The trap in its shielding (L) and the shielding with lid (R)*

3.1.4 Driving and detection coils

For the driving and detection of the magnet's oscillations, we mounted two copper coils on PEEK rods into a 3D-printed lid on the trap. The coils are 80-micron diameter insulated copper wire, wound 120 times around a 2 mm diameter PEEK rod. Their resistances (at room temperature and *in situ*, respectively) and inductances are

- Coil 1: $R_{RT} = 3.48\,\Omega$; $R_{30mK} = 27.4\,m\Omega$; $L = 18\,\mu H$
- Coil 2: $R_{RT} = 4.81\,\Omega$; $R_{30mK} = 40.4\,m\Omega$; $L = 20\,\mu H$

The copper wires were made into twisted pairs. The end of each wire was then sanded to remove the insulation, and soldered to four pins leading to separate BNC connectors outside the cryostat.

Mounted into the lid, the coils are parallel and the distance between the two coils is 4.0 mm, centre to centre.

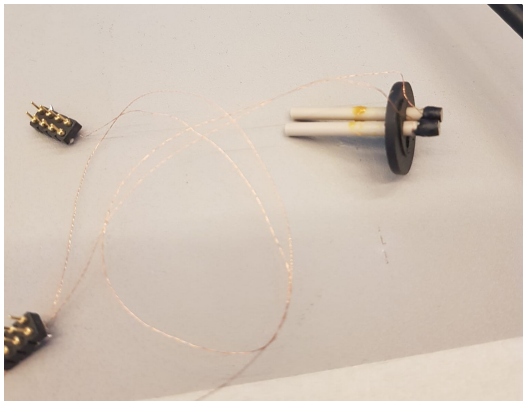

Figure 3.5: *The two coils mounted into the 3D-printed lid, and soldered each to an eight-pin connector.*

3.1.5 Expected signal

When the coil drives the magnet, a voltage is generated by self-induction.

$$U_L = i\omega LI \tag{3.1}$$

This part of the complex amplitude is imaginary. At resonance, the force on the mechanical oscillator (magnet) and its velocity are in phase

[12]. The force on the magnet is directly proportional to the coil's magnetic dipole moment and therefore the current.

$$F \propto \mu_{coil} \propto I \tag{3.2}$$

It follows that at resonance the velocity of the magnet is in phase with the current. The induced voltage from the magnet is the time derivative of the flux through the coil. Putting it all together, we derive

$$U_{ind} \propto \frac{d\Phi}{dt} \propto \frac{dB}{dt} = \frac{dB}{dx}\frac{dx}{dt} \propto v \propto F \propto I \tag{3.3}$$

We conclude that, at resonance, the self-induced signal and the magnet-induced signal are perfectly orthogonal and easily distinguished.

3.2 Racetrack Fabrication

One of the immediate goals of the Oosterkamp lab is to replace the periodic gravitational source outside of the cryostat [2] with one of a much smaller mass located within the cryostat. To this end, Stefano Goeptar and Marnix Hettema have been leading the development of a circular racetrack in which an aluminium superconducting particle is levitated by DC coils [13] [14]. The composite trap mechanism developed in our research was deemed a viable alternative for the construction of a circular racetrack.

3.2.1 Design and materials

In order to serve as a periodic gravity source for a levitated test particle, a magnet must pass a given point along the racetrack at the resonance frequency of the test particle. Previous measurements of the trap had yielded a resonance frequency of 19 Hz, so this was used for further calculations.

The shape of the racetrack is a cylindrical shell with a rounded rectangular trench. See a 3D rendering below.

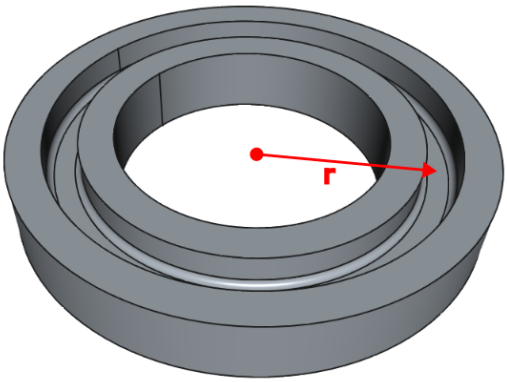

Figure 3.6: *A CAD model of the racetrack. The radius is marked.*

The width and depth of the trench are 5 mm, such that the magnet, levitating at the approximated z_0 = 2.2 mm, is about the same distance to the track's surface in three directions.
The diameter of the track had to be chosen based on the centrifugal force on the magnet at the desired frequency of revolution. The magnet's B-field starts exceeding tantalum's critical field when the magnet's COM is 1.5 mm from the surface (see section 2.1.2). The maximal centripetal force is taken to be the Meissner-effect force at this distance from the surface. This determines the orbital radius at a given frequency.

$$F_c = (\frac{1.5\,\mathrm{mm}}{2.2\,\mathrm{mm}})^{-4} \cdot F_g \Rightarrow \frac{mv^2}{r} = 4.6 \cdot mg \Rightarrow r = \frac{4.6g}{(2\pi f)^2} \tag{3.4}$$

For a frequency of revolution of 19 Hz, this gives $r = 3.2\,mm$, which would be physically impossible for a racetrack with a 5 mm-wide trench. Therefore it was determined that in the final design not one but three magnets (spaced equally around the track by a thin foil or filament) would race around the track. For the same fly-by frequency at a given point, this reduces the orbital frequency of each magnet by a factor three.
For a single magnet, the frequency is now 19 Hz/3 = 6.3 Hz and the necessary orbital radius is r = 29 mm. Since the orbital radius is 1 mm more than the radius of the racetrack, a final r = 28 mm was decided upon.

The fabrication of the racetrack was essentially identical to that of the trap. A 3D-printed mould was filled with pourable silicon. After degassing, then hardening at room temperature over a weekend, the silicon could be removed. After baking at 100 °C for 3 hours, the silicon mould

was ready for the Stycast-tantalum mixture. The mixture with 20 volume-percent tantalum was poured into the silicon mould, degassed, and left to harden overnight. It could then easily be removed from the mould. The bottom of the racetrack was flattened on a belt sander for better thermal contact.

Figure 3.7: *The racetrack (bottom) and its silicon mould (top).*

Due to loss of the Stycast-tantalum mixture during production, the bottom of the racetrack was only 3.8 mm thick, rather than the trap's 5.2 mm. This may have contributed to less reliable levitation in the racetrack than in the trap.

3.2.2 The magnet

The magnet levitated in the racetrack is identical to the magnet in the trap: a 1x1x2 mm rectangular prism shape made of two 1x1x1 mm NdFeB cubes. If a different magnet is used in the future, the consequences for levitation height, centrifugal force, and coupling to coils (both driving and detection) need to be considered.

3.2.3 Fastening, thermalisation and shielding

The racetrack was shielded by a cylindrical aluminium box with 4-mm walls, which could be mounted directly onto the mixing chamber plate

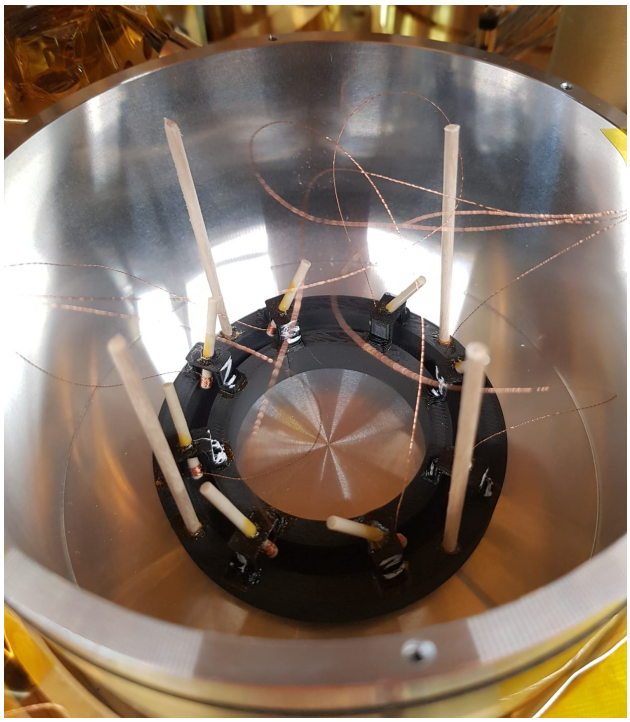

Figure 3.8: *The racetrack in its aluminium box on the mixing chamber plate.*

by 6 bolts. The cylindrical box has an aluminium which can be screwed firmly onto the box. Two holes make way for the wires of the coils, and ensure gas can escape.

Wooden rods were placed between the racetrack and the box lid so the racetrack was pushed down for good thermal contact. We covered all sides of the box in μ-metal for extra shielding.

Installation of a ceramic pedestal

Although placing the racetrack directly onto the bottom of the aluminium box provides the best thermalisation, it risks defeating entirely the goal of the SC-resin composite traps. Since a significant amount of flux can penetrate the resin, it may become trapped when the aluminium transitions to the type-I SC state. In order to minimise this flux trapping while maintaining the magnetic shielding, it would be ideal to place the racetrack exactly between the bottom and roof of the box. The challenge is to keep the racetrack thermalised.

The racetrack was heightened during the final ELSA run by putting it on a pedestal of Macor®. This was the best available thermal conductor which is an electrical insulator (since eddy current damping is to be avoided). It has a thermal conductivity of 1.46 W/mK which is slightly higher than that of Stycast. The pedestal was machined to fit snugly into the racetrack's central opening. Stycast was used to glue the racetrack to the pedestal, and a block of balsa wood was placed between the pedestal and the box lid to push the pedestal firmly against the bottom.

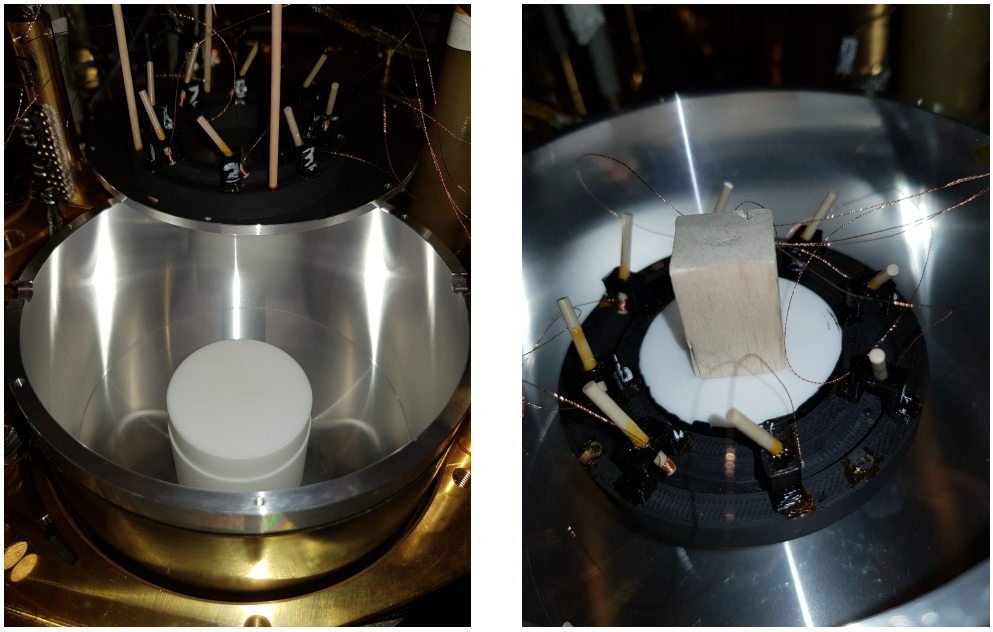

Figure 3.9: *The Macor pedestal in the aluminium box (left) and the racetrack fastened atop the pedestal (right).*

The elevation on the pedestal means the magnetic field reaching the bottom of the box is significantly weaker.

$$\frac{B_{\text{new}}}{B_{\text{old}}} = \left(\frac{d_{\text{new}}}{d_{\text{old}}}\right)^{-3} = \left(\frac{2.4 + 3.8 + 24.0}{2.4 + 3.8}\right)^{-3} = 0.009 \tag{3.5}$$

If flux trapping scales in any meaningful way with field strength, it should be significantly reduced.

3.2.4 Driving and detection coils

We made eight copper coils - 80 µm wire diameter, 80 turns around a 1 mm diameter PEEK rod. They were placed around the racetrack in 3D-printed

brackets. The brackets were glued to the racetrack with GE varnish. The coils were at a roughly 60-degree angle to the horizontal, and their bottoms aligned with the top of the racetrack trench.

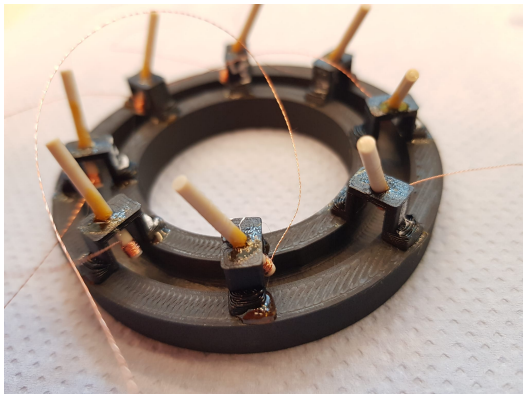

Figure 3.10: *The racetrack with eight coils, each in a bracket.*

The wires of each coil were made into a twisted pair. The ends of each pair were soldered to a block with four pins, i.e. two pins per wire. The resistances of the coils (at room temperature and *in situ*) were determined by 4-point measurements. These and their inductances are tabulated below.

Coil	R_{RT} (Ω)	R_{30mK} ($m\Omega$)	L (μH)
1	2.42	22.6	5.02
2	2.40	23.2	5.12
3	2.35	22.6	5.68
4	2.19	21.0	6.04
5	2.83	27.0	6.00
6	2.50	23.4	5.54
7	2.30	22.0	5.11
8	2.36	22.8	5.36

Table 3.1: *Resistances and inductances of racetrack coils*

The mutual inductance between coils was also determined, by sending an AC current at different frequencies through coil 1 and measuring the voltage over coil 2. The results, and a linear fit through the origin, are pictured below

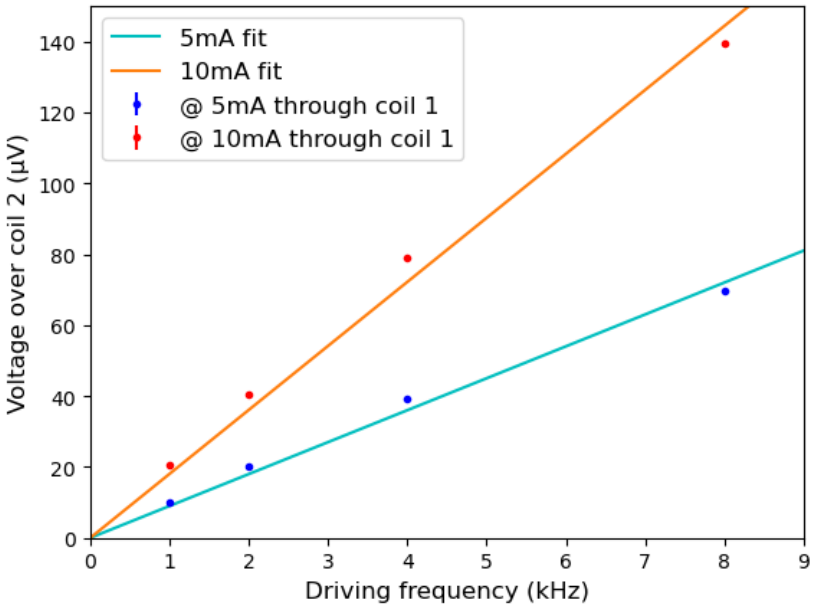

Figure 3.11: *Mutual inductance from coil 1 to coil 2 in the racetrack.*

Plugging the fitted coefficients into $M = V_2/2\pi f I_1$ yields $M = (287.0 \pm 0.4)$ nH.

3.3 Cryogenic set-up

All experiments were performed in ELSA, one of the cryostats of the Oosterkamp lab. ELSA is a dilution fridge with two pulse tubes. The experiments were placed on the mixing chamber (MC) plate. The MC plate has been shown to achieve sub-10 mK temperatures, but was more typically around 30 mK during these experiments. By disengaging one/both of the pulse tubes and activating heaters, the MC plate temperature could be raised to above 1.2K, in which case the aluminium casing of the experiment transitioned to the normal state, or above 4K, in which case the tantalum did as well.

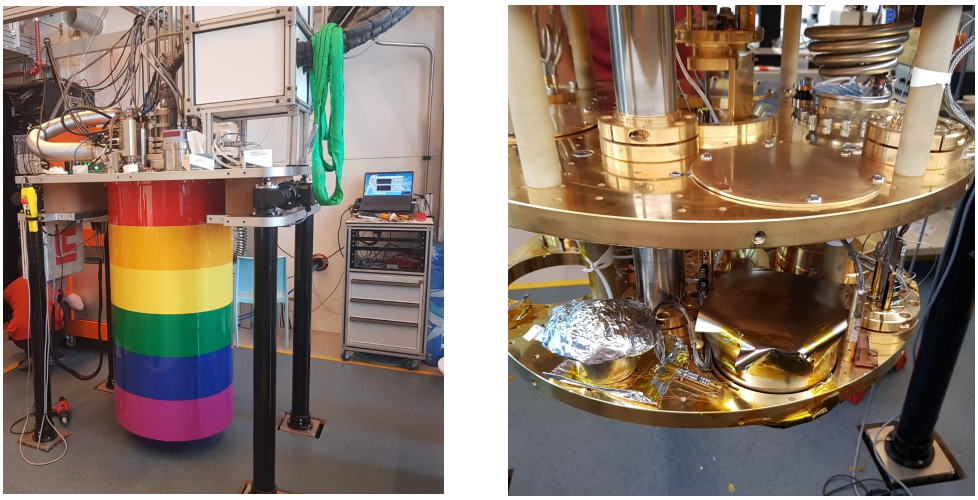

Figure 3.12: *The cryostat ELSA (left) and the experiments on the MC plate (right).*

3.4 Driving and detection

3.4.1 Magnetic driving

Single coil

For most measurements, the driving and detection were done simultaneously by a single coil. The ZI lock-in amplifier could drive the coil at a given frequency or sweep across a range of frequencies. The resistance and self-inductance of the coil gave a baseline signal of

$$U_0 = (R + i\omega L)I \tag{3.6}$$

which in practice gives a constant real-part offset during sweeps, and an imaginary-part offset which increases linearly with frequency. This can easily be distinguished from a resonance response, whose peak has an entirely real - i.e. in phase - amplitude. See an example measurement below.

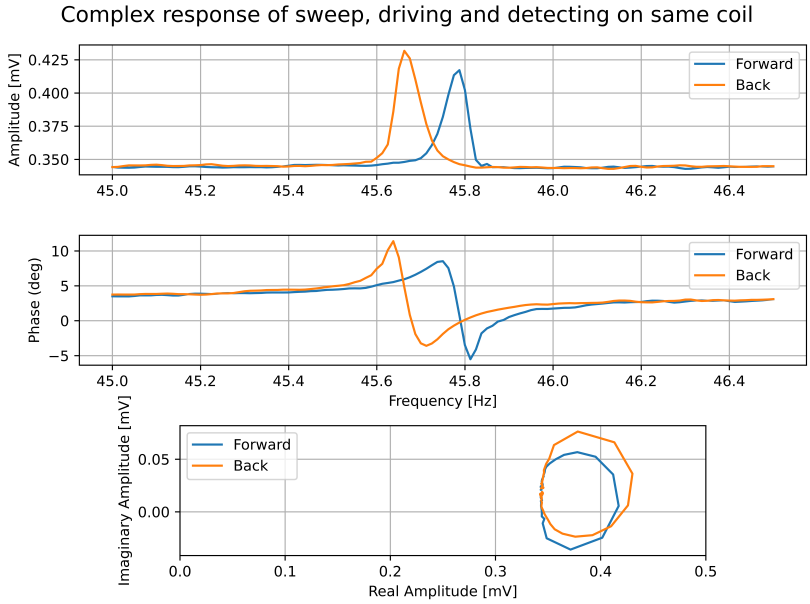

Figure 3.13: *Example measurement when driving and detection occurs on the same coil of the racetrack. Absolute amplitude, phase, and complex amplitude are shown.*

Coil-to-coil

In some cases, the driving coil and detection coil were not the same. In the racetrack, this could be used to determine on which side of the driving coil the magnet was levitating, by detecting through the coil on either side of the driving coil. None such measurements are included in the results section.

3.4.2 Voice coil driving

The magnet was also driven by a voice coil. The voice coil consists of a coil and a permanent magnet attached to a block of stainless steel, which was placed on top of the cryostat. Driving the coil with AC causes the mass to oscillate in the z-direction and shake the entire cryostat. This was especially advantageous when we tried to confirm levitation in the racetrack, since we did not know the location of the magnet and therefore which magnetic driving coil to use. To begin with, multiple detection coils were connected in parallel to establish whether there was levitation anywhere in the region. Then single detection coils could be measured to determine the magnet's location.

Figure 3.14: *The voice coil fastened on top of the cryostat.*

3.4.3 Detection and amplification

To detect the magnet's motion, in each case the voltage difference over a detection coil was measured. The positive and negative sides of the coil were connected to the corresponding input of a Falco Systems Low Noise Preamplifier. The preamp amplified the signal difference by a gain of 100-100k, but typically 1k or 10k for these measurements. The preamplified signal was then fed back into the ZI lock-in amplifier.

3.4.4 Q factor and energy coupling

The signals measured by the lock-in amplifier are voltages with complex amplitudes. From these, the Q factor and energy coupling β^2 of each resonance peak can be determined.

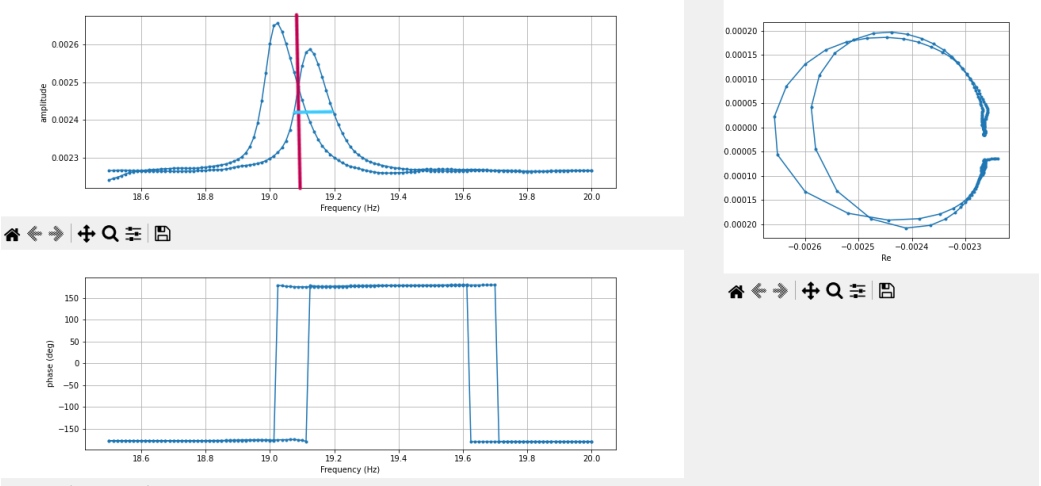

Figure 3.15: *Sweep across a resonance peak at* (19.1 ± 0.1) Hz. *The frequency is marked in red, the full width at half height* Δf *is marked in blue. Note also that the resonance is a circle in the complex plane.*

The Q factors are determined from the resonance peaks by

$$Q = \frac{f}{\Delta f} \tag{3.7}$$

With f the frequency of the resonance and Δf the full width at half height. In all cases, the resonances showed non-linearity, meaning that the forward and backward sweeps did not return precisely the same frequency and amplitude. For consistency, all reported frequencies are those where the two resonance peaks intersect, as marked in red in the above graph. In each case, Δf was taken from the forward sweep, as marked in blue above. For the example resonance above, the Q factor is determined as

$$Q = \frac{f}{\Delta f} \approx \frac{(19.1 \pm 0.1)\,\text{Hz}}{(0.14 \pm 0.02)\,\text{Hz}} = (1.4 \pm 0.2) * 10^2$$

It must be admitted that this calculation method of the Q factor is done by eye and not very precise. For our order-of-magnitude purposes, it is sufficient.

The factor β^2 is a measure of the coupling between the energy in the coils and the energy of the magnet harmonic oscillator. It is defined as [2]

$$\beta^2 = \frac{E_{\text{coil}}}{E_{\text{HO}}} = \frac{LI^2}{kx^2} \tag{3.8}$$

With L the coil's inductance, I the induced current, k the spring constant of the magnet's oscillating mode, and x the oscillation's amplitude. For the non-superconducting pick-up coils, β^2 is related to Q by

$$Q\beta^2 = \frac{I_{\text{response}}}{I_{\text{drive}}} = \frac{V_{\text{offset}}/\omega L}{V_{\text{circle}}/\omega L} = \frac{V_{\text{offset}}}{V_{\text{circle}}} \tag{3.9}$$

Here V_{offset} is the voltage due to the self-induction of the coil. As explained in section 3.1.5, this is the imaginary part of the complex voltage. V_{circle} is the amplitude of the resonance peak, most easily determined by the diameter of the complex circle. The complex plane from the figure above is here replicated with useful annotations.

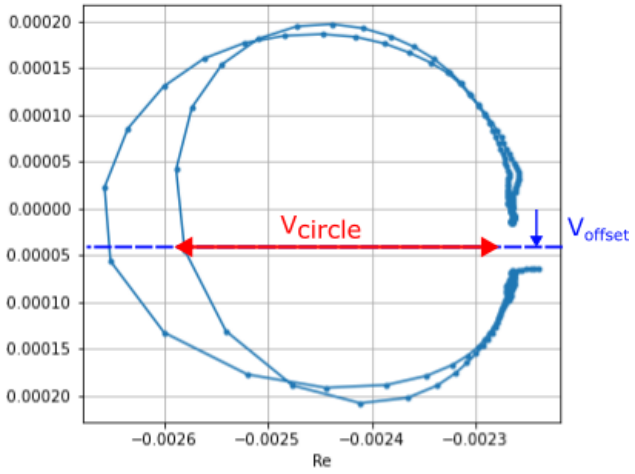

Figure 3.16: *The complex voltage signal of a resonance peak. V_{circle} is the diameter of the circle, marked in red. V_{offset} is the imaginary offset due to the coil's self-induction.*

In the results section, β^2 is in each case calculated as

$$\beta^2 = \frac{1}{Q}\frac{V_{\text{offset}}}{V_{\text{circle}}} \tag{3.10}$$

using the voltages from the forward sweep.

3.4.5 Calibration

For non-superconducting pick-up coils, the induced voltage due to the oscillating magnet is

$$V = -\frac{d\Phi}{dt} = \omega I L \tag{3.11}$$

This can be combined with equation (3.8) to calibrate the voltage amplitude of the resonance peak and the oscillation amplitude.

$$\frac{V_{\text{circle}}^2}{x^2} = \frac{\omega^2 I^2 L^2}{x^2} = \omega^2 L k \beta^2 = \omega^2 L k \frac{1}{Q} \frac{V_{\text{offset}}}{V_{\text{circle}}} \tag{3.12}$$

Since k depends on the mode of oscillation, the mode needs to be known when calculating the oscillation amplitude. There is currently no way to assign resonance peaks to particular oscillation modes. Therefore, oscillation amplitudes are not calculated in the results section below. Some steps towards these calculations are suggested in the outlook section.

Chapter 4

Results and Discussion

Due to incorrect saving of files, much of the early raw data of sweeps over resonance peaks was lost. Where possible, fresh graphs were generated from the original data, but in some places screenshots taken during the measurements had to be used. Later data, including all measurements on the racetrack, remains available.

4.1 Levitation in powder trap

We confirmed whether the magnet levitated in the trap by looking for resonances. By driving the coil at different frequencies and looking at the response voltage in the same coil, we could identify resonance peaks. Not all peaks are due to resonances: true resonance peaks are circles in the complex plane. From earlier calculations, resonances were expected on the order of 10 Hz. For this reason, exploratory measurements tended to sweep from 1 Hz to 50 Hz or so, although higher frequencies were also checked occasionally. The graph below shows an early sweep on the coil in the trap. It shows at least three resonance peaks: some of the first evidence that the magnet indeed levitated.

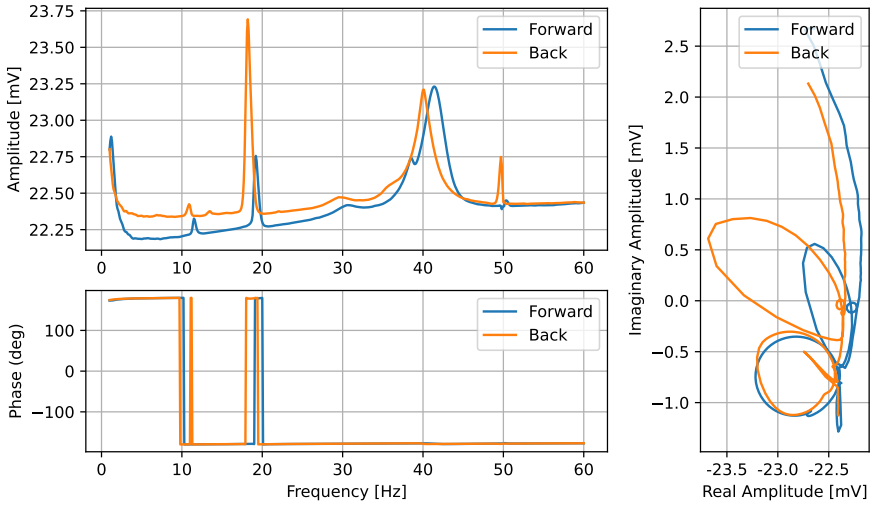

Figure 4.1: *Amplitude, phase, and complex response of coil in trap, swept over driving frequencies. Three resonance peaks and their characteristic complex circles can be identified.*

Sweeps with higher frequency resolution and lower driving voltage were used to identify the frequencies, Q factors, and energy couplings of individual peaks. This is needed because the width and non-linearity of peaks depend on the resolution and driving voltage of the sweep. They appear to approach a 'true' value asymptotically as sweeps become finer.

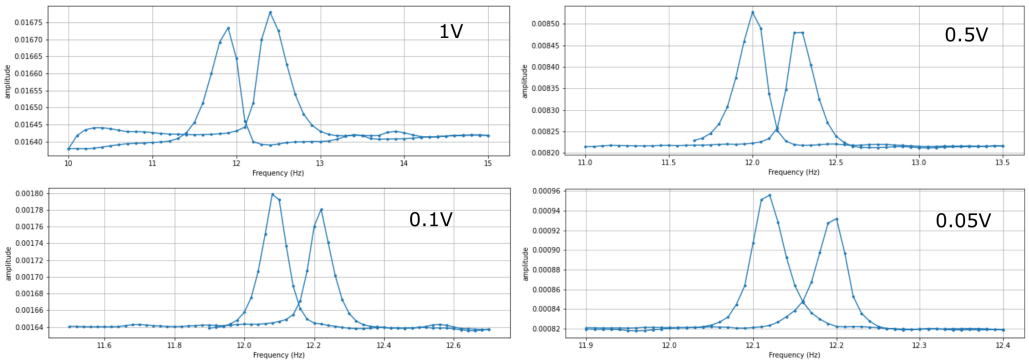

Figure 4.2: *Finer sweeps on a mode in the powder trap. The driving voltage is noted in each graph. Note that the frequency resolution increases: the frequency range narrows, while the number of data points is constant. The width of the peak and the separation between the forward and backward sweep peaks reduce.*

4.1.1 Mode frequencies

The state of the aluminium shielding influenced the resonance frequencies. Presumably the Meissner effect from SC aluminium contributed a restoring force, increasing frequencies. Since the aluminium was wrapped around but not above or below the trap, horizontal modes should be most affected. The figure below shows that some frequencies differ a great amount above and below the T_C of aluminium, whereas other did not noticeably change.

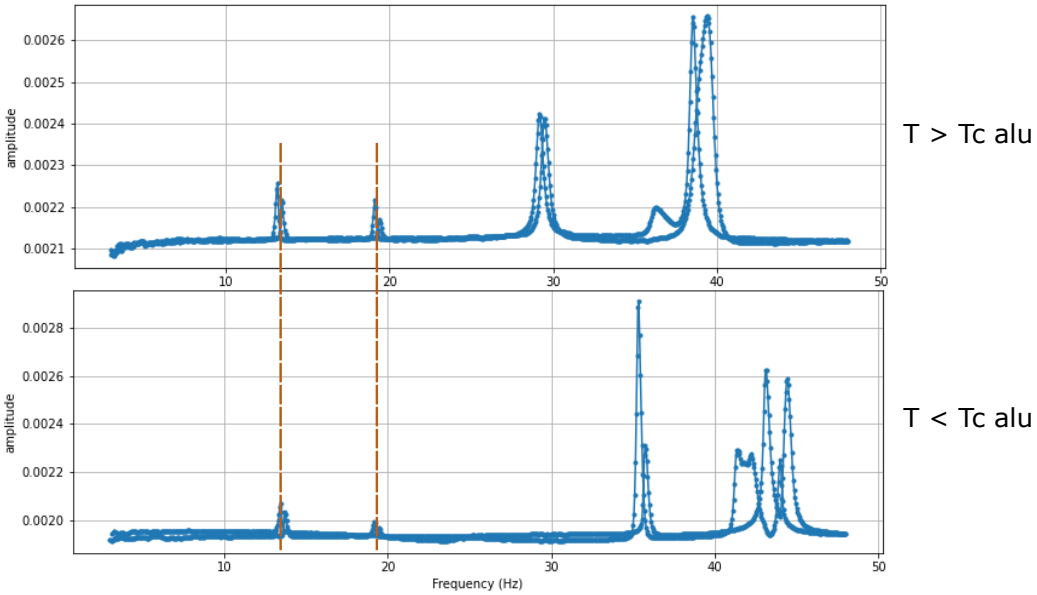

Figure 4.3: *Resonance frequencies in the trap, above and below the T_C of aluminium, respectively. Dashed lines illustrate the consistency of two modes. Two other mode frequencies increase significantly as aluminium achieves the SC state.*

Below are tabulated the frequencies, Q factors and β^2 couplings in the trap. Each run is a new cooldown of the cryostat. Between runs, adjustments were made to the trap, such as the adding of new aluminium shielding. All Q factors are *as measured*. They depend on the resolution, bandwidth, and driving amplitude of the sweep. The Q factors below are taken from the highest-resolution sweep available.

Run	f (Hz)	Q	β^2	Notes
1	(11.2 ± 0.2)	46	0.05	Copper cladding
	(14.1 ± 0.1)	36	0.16	
	(19.13 ± 0.03)	192	0.04	
	(40 ± 2)	15	0.08	
2a	(13.29 ± 0.04)	333	0.014	Aluminium shielding, above T_C
	(19.24 ± 0.06)	276	0.006	
	(29.3 ± 0.3)	49	0.06	
	(39.0 ± 0.5)	49	0.15	
2b	(13.58 ± 0.05)	195	0.023	Aluminium shielding, below T_C
	(19.28 ± 0.04)	275	0.01	
	(35.54 ± 0.03)	118	0.1	
	(43.1 ± 0.1)	86	0.05	
3	(13.10 ± 0.05)	218	0.02	Aluminium shielding, below T_C
	(19.60 ± 0.05)	393	0.006	
	(41.10 ± 0.05)	294	0.01	
	(50.0 ± 0.5)	84	0.02	

Table 4.1: *Frequencies, Q factors, and energy couplings in the trap*

4.2 Levitation in racetrack

After measuring sweeps on all eight coils, peaks were found when measuring with coil 5, the coil under which the magnet was originally placed.

4.2.1 Mode frequencies

First, to confirm levitation anywhere in the racetrack, we drove the who cryostat with the voice coil. Detection was done by four coils in parallel (numbers 2-5). Two resonance peaks could be discerned.

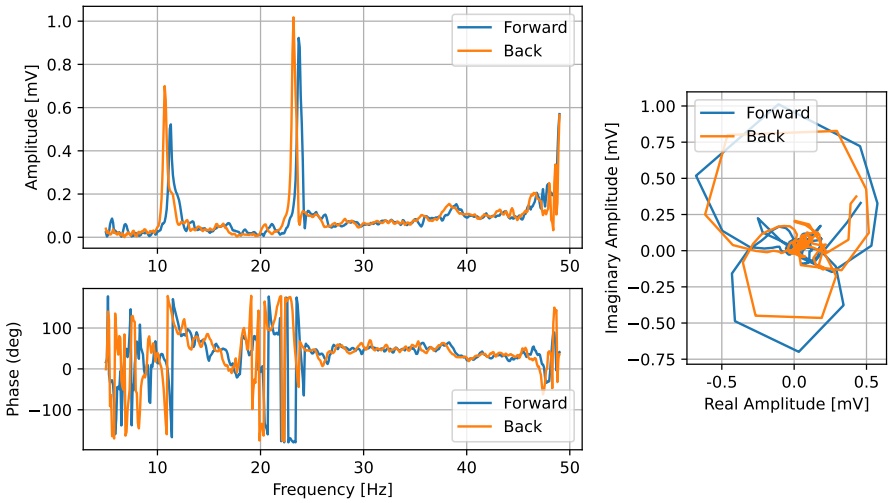

Figure 4.4: *Sweep driven by the voice coil and detected by coils 2-5 in parallel. The two resonance peaks indicate that the magnet is levitating in proximity to one of these coils.*

After driving with the voice coil, we switched to magnetic driving with individual coils. Four resonance peaks could be discerned when driving magnetically with coil 5 and detecting with the same coil.

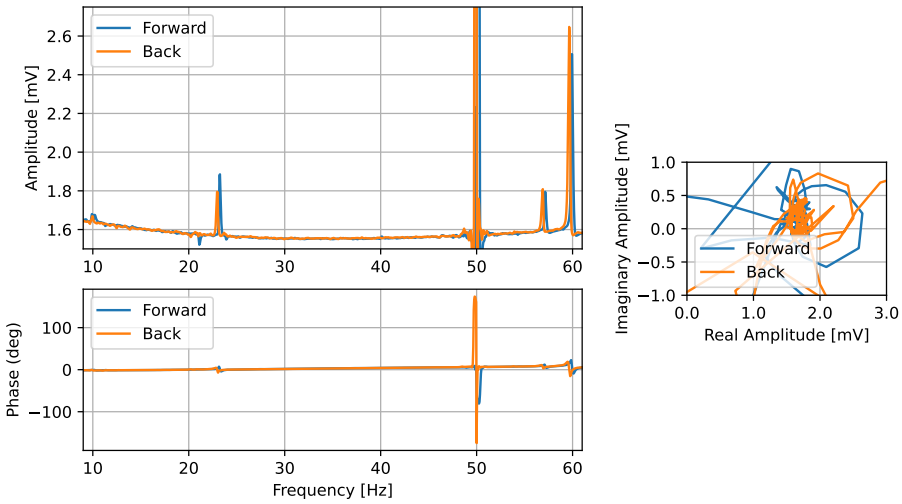

Figure 4.5: *Four resonance peaks in the racetrack. They can be seen at 10 Hz, 23 Hz, 57 Hz, and 60 Hz. The power grid signal at 50 Hz should be ignored.*

We also performed a sweep above the T_C of aluminium, at about 1.3 K. Between two sweeps, the MC-plate temperature was increased to above the T_C of tantalum - to about 6 K. Then it was cooled back to 1.3 K. Below are the sweeps before and after.

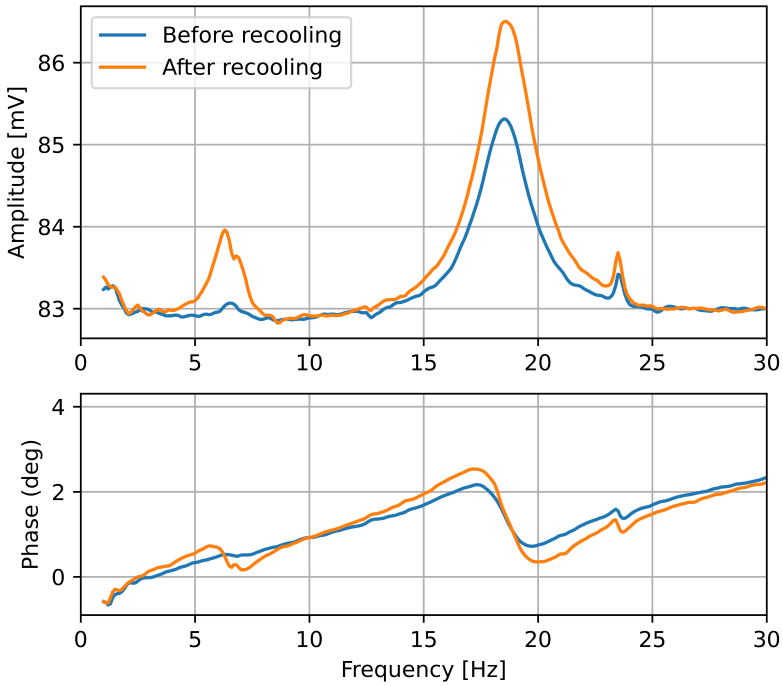

Figure 4.6: *Sweeps above the T_C of aluminium, showing three resonance peaks. Sweeps were performed before and after heating above the T_C of tantalum. Only forwards sweeps are shown, for clarity.*

As a sanity check, we performed a sweep while the MC-plate temperature was 6 K. Since the tantalum is then not SC, the magnet should not be levitating and no resonances should be found. No resonances were found.

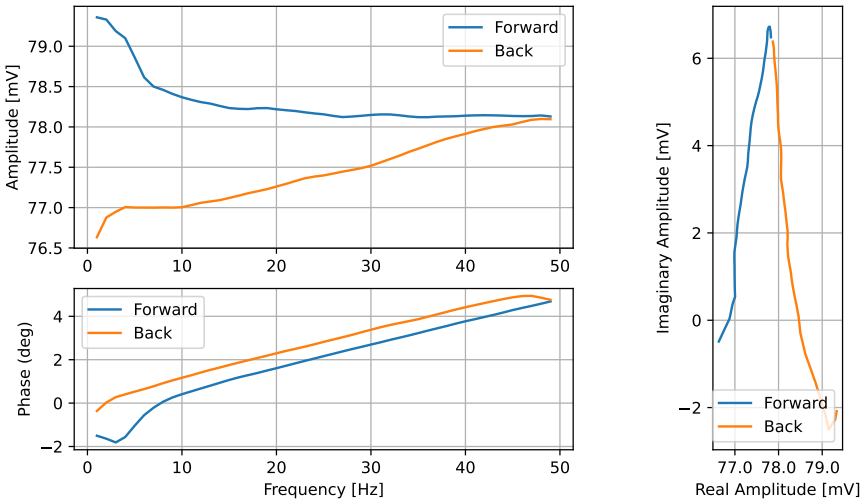

Figure 4.7: *A broad sweep while the MC-plate was around 6 K. No peaks can be seen, indicating that resonances only appear with SC tantalum, and that they originate from a levitating magnet. The near-vertical lines in the complex plane are also a nice illustration that the self-induction, which scales with frequency, gives an imaginary voltage signal.*

Below is a table of the resonance frequencies measured in the racetrack across cryostat runs. Their Q factors and β^2 couplings are included. All these measurements are below the T_C of aluminium and without DC offsets on the coils (see also section 4.2.2).

Run	f (Hz)	Q	β^2	Notes
1	(10.02 ± 0.03)	251	0.1	
	(23.05 ± 0.04)	577	0.03	
	(57.0 ± 0.2)	286	0.003	
	(59.8 ± 0.1)	300	0.02	
2a	(21.75 ± 0.02)	484	0.04	
	(45.79 ± 0.04)	917	0.005	
	(54.35 ± 0.05)	777	0.001	
2b	(7.78 ± 0.08)	98	0.05	
	(21.97 ± 0.03)	275	0.09	
	(44.1 ± 0.1)	368	0.02	
3	(23.65 ± 0.03)	592	0.0006	Ceramic pedestal added
	(45.53 ± 0.03)	570	0.04	

Table 4.2: *Frequencies, Q factors, and energy couplings in the racetrack*

Once the ceramic pedestal was added, only two resonance frequencies could be found. This may indicate that the aluminium shielding was providing some of the Meissner levitation for the magnet. Now that the racetrack is farther from the aluminium, the magnet may only partially lift off, perhaps standing on one of its faces. This would only allow rotational modes, not translational.

4.2.2 Motion along the racetrack

By tilting the cryostat

The cryostat ELSA could be tilted by manually turning an axle, which extends the screw-thread legs on one side. If the magnet levitated unconstrained, the tilt should have caused it to move to the lowest point. At least, there would be a significantly lower coupling measured at coil 5, which was halfway up the slope - neither at the highest point nor the lowest. Below are shown sweeps across a 10 Hz mode when the cryostat was at about 0.9° and at about 0.2° to the horizontal, respectively.

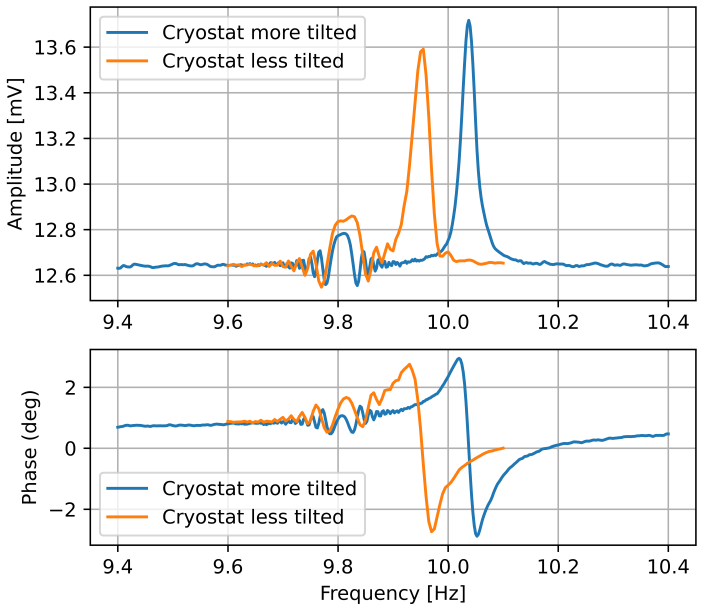

Figure 4.8: *A resonance peak when the cryostat ELSA was more tilted or less so. Driven and detected on racetrack coil 5. Only forward sweeps are shown, for clarity. The signal at 9.8 Hz is a harmonic of the pulse tube.*

Although there is a small, significant change in the resonance frequency, the coupling is not significantly different. If the magnet had moved even one coil along, the signal should have been lost at coil 5. The small change in frequency is to be expected, since at a different angle the Meissner repulsion is working against a different component of gravity.

By applying DC driving offsets

When a DC voltage is applied on the driving/measurement coil, it effectively behaves as an additional permanent magnet. This should shift the equilibrium position of the levitating magnet towards or away from the coil. Such a shift should significantly increase or decrease the coupling (and therefore sweep amplitudes) when driving magnetically. Below are the results of such a measurement.

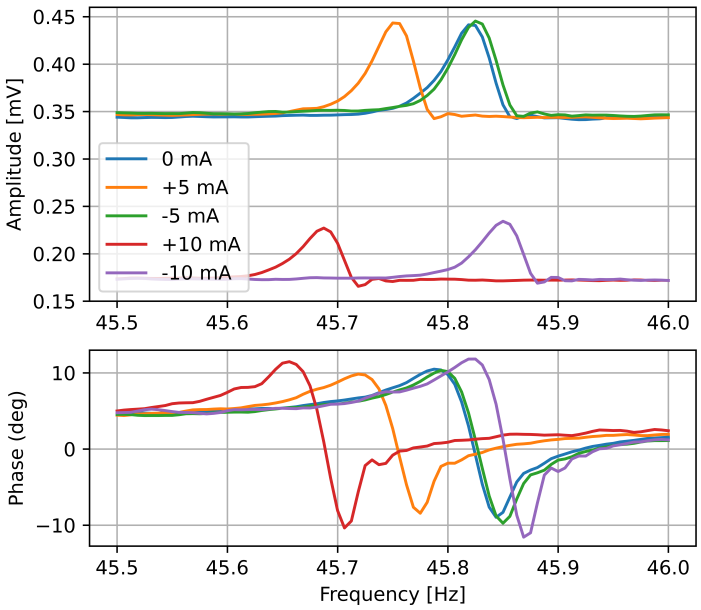

Figure 4.9: *A resonance peak when DC offsets were applied to driving/measurement coil 5. The lowered 'baseline' voltage with a* $\pm$ 10 mA *offset suggests a change to the self-induction, not the magnet signal.*

We can observe a significant shift in resonance frequency due to the DC offsets. The direction of this shift also depends on the sign of the offset. However, the coupling barely changes, even though this should be highly sensitive to coil-magnet separation. This suggests the magnet does not shift along the racetrack. Perhaps its equilibrium angle rather than position can account for the frequency change.

Chapter 5

Outlook

5.1 Limits on Q factors and plausible improvements

In this research, we have seen that the Q factors as measured in the traps are orders of magnitude lower than they might be. We assume we have accounted for all relevant dissipation mechanisms, but there might be others of which we are unaware. Apart from unknown dissipation, low Q factors may point to (a) fundamentally different behaviour in powder SC systems in contrast to bulk SC systems, or (b) room for optimisation in eliminating flux trapping.

(a) It is possible that a powder composite trap cannot support high-Q factor resonance modes. The reason is this: in a composite trap, SC particles are distributed throughout the insulator, perhaps quite heterogeneously. In any case, this means the SC does not look the same from up close as it does from far away. As the magnet oscillates, its position to the SC particles changes, which may change the local density of SC in the composite, etc. Such effects can result in a non-linear Hooke's law. With an ill-defined spring constant, there are ill-defined eigenfrequencies. The result is broadened resonance peaks and lower Q factors.

(b) Flux trapping may still be happening in the powder particles. If a powder particle is much larger than an SC grain, there may be just as much flux trapping as in the bulk. In order to eliminate this, we can use

finer SC powder in the upcoming traps. Not only might this practically increase Q factors, but it may serve as a platform for understanding flux trapping. From the powder size's impact on flux trapping effects (low Q factor, frequency drift, frequency predictability, etc.) we may learn the size of SC grains and develop a model for the escaping of trapped flux.

5.2 Identifying modes and calculating amplitudes

As discussed in section 3.4.5, it is currently not possible to calculate the amplitude of the magnet's oscillation, because the calibration of signal voltage to oscillation amplitude depends on the spring constant. Therefore, a method is required to link particular resonance peaks to particular translational/rotational modes. Some suggestions for approaching this in future:

- **Simulations**. Currently, no COMSOL simulations have been designed for the magnet's motion in the powder trap or racetrack. This may be valuable in order to understand the system's properties (such as a possible inherent upper bound to Q factors), as well as a more rigorous prediction of resonance frequencies than the infinite-plane approximations made here.

- **Coil placement.** Different oscillation modes change the magnetic field around the magnet in different ways. Pick-up coils at different places will have different flux changes due to the different oscillation modes. By comparing signal amplitudes from these coils, the frequencies could be linked to modes. This may be more realistic when we switch to SC pick-up loops for SQUID measurements, since they are much smaller than the coils we have used in the powder trap so far.

- **Influence of SC metals.** As noted in section 4.1.1, the Meissner effect from SC shielding can strongly influence resonance frequencies. This may be used to our advantage. We could strategically place pieces of metal on the x, y, and z-axes with respect to the magnet. By noting which resonance frequencies change when these pieces become SC, we could identify the modes. To do this in a single cryostat run, the pieces would have to be of different metals such that they become SC at different temperatures.

5.3 Proposed next steps for racetrack development

There are currently two problems with the racetrack. Firstly, we are not confident that the magnet lifts off at every cooldown. Secondly, we have not succeeded in sending the magnet around the racetrack.

In order to make the levitation of the magnet in the racetrack more reliable, we can learn from the composite trap. In the trap, the magnet levitated every time; there would not have been four resonance modes otherwise. The trap has no SC cladding directly below it, so that cannot be the difference. The problem might be thermalisation. It probably isn't, because the two resonances measured in the last racetrack run only appeared below 4K; it clearly arises from the tantalum going SC. The only difference left between the trap and the racetrack is the thickness of the bottom. Making a new racetrack with more composite in the same mould could already suffice. Better cleaning protocols for the racetrack and magnet could prevent sticking.

To send the magnet around the racetrack, we can make two improvements. The first is to increase the Q factors. If flux trapping is locking the magnet in place, we could use finer SC powder to reduce this. The second improvement is stronger and more optimally placed driving coils. The system does not tolerate a lot more Joule heating, so we need to design coils with a stronger dipole without much higher currents. The placement is also important. What angle optimises the force on the magnet? How close can we get? We could even consider wrapping a coil around the trench of the racetrack; this would generate a B-field precisely along the trench. Because flux can penetrate the composite, this field can reach the magnet from all sides, not just from the top, as would have been the case with a bulk SC.

Chapter 6

Conclusion

In this research, we successfully levitated magnets in novel superconducting composite traps. A 1x1x2 mm NdFeB magnet could be levitated in a trap composed of Stycast resin with 18% tantalum powder by volume. Levitation was confirmed by the presence of 4 resonance peaks in the response to an AC driving coil, each being a circle in the complex plane. The quality of the resonances is poor, with Q factors on the order of 100s, never exceeding 1000. We explored relevant dissipation mechanisms and could not conclude which primarily limited Q factors. Poor Q factors may be inherent to the tantalum-resin composite system, either by increased SC surface area or non-linearity of the harmonic oscillation.

We also constructed a racetrack of the same tantalum-resin composite, with 20% tantalum powder by volume. Levitation was successful when the racetrack was placed directly onto superconducting aluminium shielding, but could not be confirmed when the racetrack was separated from the shielding by a ceramic block. We have not managed to propel the magnet around the racetrack, or even a measurable distance from any given coil. Neither a DC offset on the driving coil(s) nor a tilt of the cryostat caused a significant change in the coupling to the pickup coil, indicating the magnet remained in place.

Larger and more effectively placed driving coils may allow the propulsion of the magnet around the racetrack. It may then serve as a periodic source mass for a small-gravity measurement on the Zeppelin. It would be 10^{-5} as massive as the source mass used in the previous Zeppelin experiment, and may be a significant step towards the measurement of gravity from a source mass in a spatial superposition.

Chapter 7

Acknowledgements

I am grateful to many people for their help during this research project. Firstly, Tjerk Oosterkamp and Dennis Uitenbroek for their constant efforts to keep this project going with focus and purpose. Secondly, to the dedicated people of the Fine Mechanical Department, especially Merlijn Camp and Martijn Wilcox, without whose creations this project would have been impossible. Thirdly, to my fellow students in ELSA's corner of the Oosterkamp lab: Winesh Nathie, Marnix Hettema, and Mart Laurman. I also want to thank the Oosterkamp lab's PhD candidates - Jurriaan Langendorff, Koen van Deelen, and Loek van Everdingen - for their expertise and guidance. All members of the bi-weekly "graviteitengroep" are due thanks for their eagerness to think along.

Chapter 8

Appendix A: simplified geometries of trap and racetrack

Here we include simplified geometries for the trap and the racetrack, and the magnet's position levitating in them. These are side views. They are not to scale, but relevant distances are labelled in millimetres.

Trap

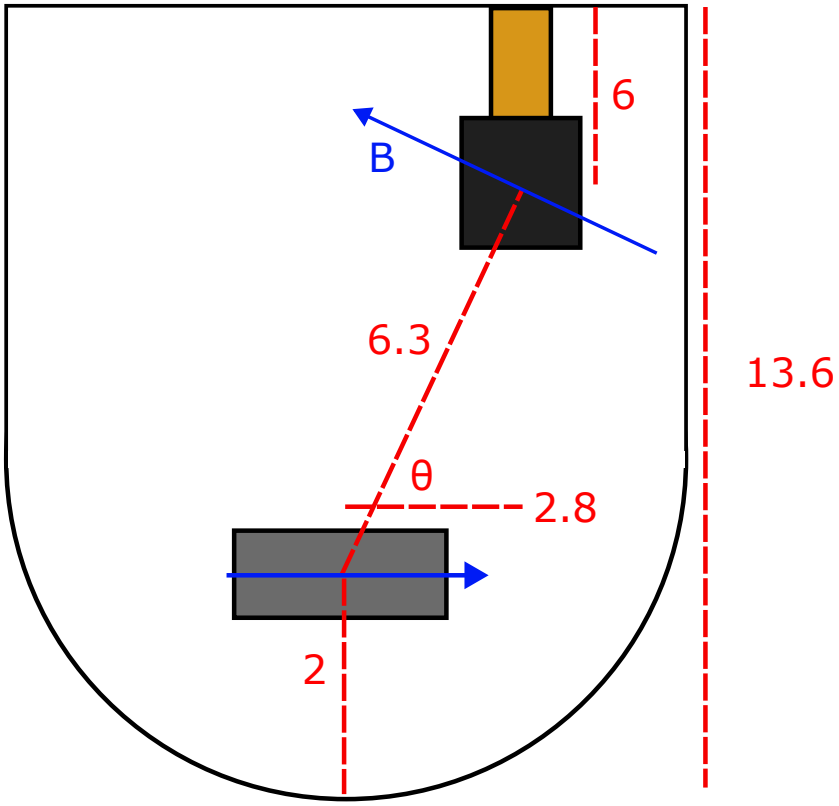

Figure 8.1: *Simplified geometry of the trap. Levitation height based on infinite-plane approximation for a 1x1x2 mm magnet. The magnetic field from the magnet is approximated as a spherical shell and is therefore orthogonal to the distance vector.*

The flux through the coil is then

$$\Phi = \cos(\theta) ANB = 0.45 \cdot \pi (1.5\,\mathrm{mm})^2 \cdot 120 \cdot \frac{B_r}{2} \left(\frac{d}{1\,\mathrm{mm}} \right)^{-3}$$

with d the distance between the centre of the magnet and the centre of the coil. The induced voltage can be found by

$$V = -\frac{d\Phi}{dt} = -\frac{d\Phi}{dz}\frac{dz}{dt}$$

from which equation (2.30) can be retrieved.

Racetrack

Below is the simplified geometry in the racetrack, assuming the magnet levitates directly under a pick-up coil.

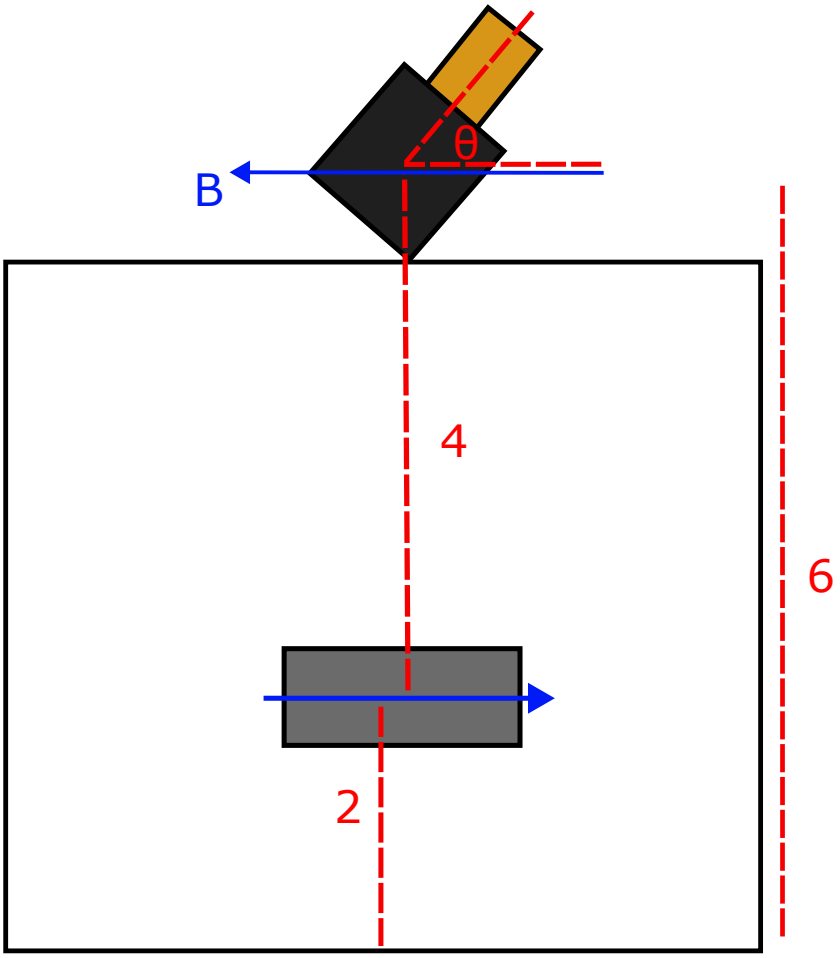

Figure 8.2: *Simplified geometry of the racetrack. Levitation height based on infinite-plane approximation for a 1x1x2 mm magnet. The coil is at an angle $\theta = 60°$ to the horizontal.*

The flux through the coil is then

$$\Phi = \cos(\theta) ANB = 0.5 \cdot \pi (1\,\text{mm})^2 \cdot 80 \cdot \frac{B_r}{2} \left(\frac{d}{1\,\text{mm}} \right)^{-3}$$

with d the distance between the centre of the magnet and the centre of the coil. Equation (2.31) can then be retrieved by finding the induced voltage as previously.

Bibliography

[1] QuTech. qutech.nl/quantumlimits/Research, Dec 2024.

[2] Tim M. Fuchs, Dennis G. Uitenbroek, Jaimy Plugge, Noud van Halteren, Jean-Paul van Soest, Andrea Vinante, Hendrik Ulbricht, and Tjerk H. Oosterkamp. Measuring gravity with milligram levitated masses. *Science advances*, 10(8):eadk2949–, 2024.

[3] Winesh Winay Nathie. Analysis on the frequency stability of the meissner levitated magnetic zeppelin. Bachelor's thesis, Leiden University, 2025.

[4] Michael. Tinkham. *Introduction to superconductivity*. Dover Publications, Mineola, NY, 2nd ed., reprint. edition, 2004.

[5] Collins Dictionary. Superconductor definition in american english — collins english dictionary, 2025.

[6] J. G. C. Milne. Superconducting transition temperature of high-purity tantalum metal. *Phys. Rev.*, 122:387–388, Apr 1961.

[7] T.J. Greytak and J.H. Wernick. The penetration depth in several hard superconductors. *Journal of Physics and Chemistry of Solids*, 25(6):535–542, 1964.

[8] Dennis Uitenbroek. Meissner levitating micro particle. Master's thesis, Leiden University, 2022.

[9] David J. Griffiths. *Introduction to Electrodynamics, Fourth Edition*, chapter 5, page 264. Pearson, 2013.

[10] Francis J. Headley. Magnetic dipole trapping potential between infinite superconducting plates, 2025.

[11] Lars Seldenthuis. Levitating a milligram gravity source. Bachelor's thesis, Leiden University, 2024.

[12] Robert E Coleman. Vibration theory. www.signalysis.com/white-papers/vibration-theory.

[13] Stefano Goeptar. Developing a circular magnetic field track for a levitated superconductor. Bachelor's thesis, Leiden University, 2025.

[14] Marnix Hettema. Meissner levitated superconductor in a circular trap. Bachelor's thesis, Leiden University, 2025.